

Robust Human Motion Tracking Using Wireless and Inertial Sensors

by

Paul Kisik Yoon

B.A.Sc., Simon Fraser University, 2013

Thesis Submitted in Partial Fulfillment of the
Requirements for the Degree of
Master of Applied Science

in the

School of Mechatronic Systems Engineering
Faculty of Applied Sciences

© Paul Kisik Yoon 2015

SIMON FRASER UNIVERSITY

Fall 2015

All rights reserved.

However, in accordance with the *Copyright Act of Canada*, this work may be reproduced, without authorization, under the conditions for "Fair Dealing." Therefore, limited reproduction of this work for the purposes of private study, research, criticism, review and news reporting is likely to be in accordance with the law, particularly if cited appropriately.

Approval

Name: Paul Kisik Yoon
Degree: Master of Applied Science
Title: *Robust Human Motion Tracking Using Wireless and Inertial Sensors*
Examining Committee: Chair: Woo Soo Kim
Assistant Professor

Edward Park
Senior Supervisor
Professor

Bong-Soo Kang
Supervisor
Professor
Hannam University

Kevin Oldknow
Internal Examiner
Lecturer

Date Defended/Approved: Dec. 7, 2015

Ethics Statement



The author, whose name appears on the title page of this work, has obtained, for the research described in this work, either:

- a. human research ethics approval from the Simon Fraser University Office of Research Ethics,

or

- b. advance approval of the animal care protocol from the University Animal Care Committee of Simon Fraser University;

or has conducted the research

- c. as a co-investigator, collaborator or research assistant in a research project approved in advance,

or

- d. as a member of a course approved in advance for minimal risk human research, by the Office of Research Ethics.

A copy of the approval letter has been filed at the Theses Office of the University Library at the time of submission of this thesis or project.

The original application for approval and letter of approval are filed with the relevant offices. Inquiries may be directed to those authorities.

Simon Fraser University Library
Burnaby, British Columbia, Canada

update Spring 2010

Abstract

Recently, miniature inertial measurement units (IMUs) have been deployed as wearable devices to monitor human motion in an ambulatory fashion. This thesis presents a robust human motion tracking algorithm using the IMU and radio-based wireless sensors, such as the Bluetooth Low Energy (BLE) and ultra-wideband (UWB). First, a novel indoor localization method using the BLE and IMU is proposed. The BLE trilateration residue is deployed to adaptively weight the estimates from these sensor modalities. Second, a robust sensor fusion algorithm is developed to accurately track the location and capture the lower body motion by integrating the estimates from the UWB system and IMUs, but also taking advantage of the estimated height and velocity obtained from an aiding lower body biomechanical model. The experimental results show that the proposed algorithms can maintain high accuracy for tracking the location of a sensor/subject in the presence of the BLE/UWB outliers and signal outages.

Keywords: Bluetooth low energy (BLE); human motion tracking; inertial measurement unit (IMU); sensor fusion; ultra-wideband (UWB)

Acknowledgements

I would like to express my deepest gratitude to my senior supervisor, Dr. Edward Park, for giving me an opportunity to participate in this project and providing guidance throughout my studies. He has been an inspiring mentor since 2009 when I first started my co-op with him. He has taught me important methodological and technical skills necessary for research excellence: (i) conducting great research, (ii) writing good research papers, and (iii) giving great research talks. He has patiently assisted and pushed me in the preparation of this thesis and the associate works.

I would like to sincerely thank my supervisor, Dr. Bong-Soo Kang, for mentoring me as a Visiting Professor. He has been knowledgeable in robotics and guided me this thesis and the associate works during my studies. I am grateful for my examiner, Dr. Kevin Oldknow, for taking his time for examining this thesis work. He has been a great instructor for his clear and informative lectures. I enjoyed learning robotics from his manufacturing course. I would like to sincerely thank Dr. Woo Soo Kim for serving the chair of my committee member. During my undergraduate studies, he was a very kind professor providing me an opportunity to learn the emerging fields of nanotechnology.

I would like to thank Shaghayegh Zihajehzadeh, Darrell Loh, Matthew Lee, Magnus Musngi, Omar Aziz, and Reynald Hoskinson at the SFU Biomechatronic Systems Lab (BSL). They have provided me with many useful feedback and suggestions throughout my studies. I would like to especially thank Shaghayegh for providing me the relevant theories, knowledge, and background literature on this thesis and the associate works and supporting my research with valuable advice. I would like to thank the Natural Sciences and Engineering Research Council of Canada (NSERC) for funding this research and financially supporting me.

Last, but not least, I would like to sincerely thank my amazing family for their love and encouragements as I complete this work.

Table of Contents

Approval.....	ii
Ethics Statement.....	iii
Abstract.....	iv
Acknowledgements.....	v
Table of Contents.....	vi
List of Tables.....	viii
List of Figures.....	ix
List of Acronyms.....	xi
Nomenclature.....	xii

Chapter 1. Introduction	1
1.1. Overview	1
1.2. Literature Survey	2
1.3. Objective	4
1.4. Contributions	5
1.5. Thesis Outline	6

Chapter 2. Adaptive Kalman Filter for Indoor Localization Using BLE and IMU.....	7
2.1 Introduction.....	7
2.2 Methodology.....	7
2.2.1 Attitude and Yaw Kalman Filters.....	8
2.2.2 Trilateration	8
2.2.3 Position Kalman Filter.....	11
2.3 Experimental Setup and Protocol	13
2.3.1 Experimental Setup	13
2.3.2 Experimental Protocol.....	15
2.4 Experimental Results and Discussion.....	17
2.5 Conclusion.....	20

Chapter 3. Robust Biomechanical Model-based Motion Tracking of Lower Body Using UWB and IMU	21
3.1 Introduction.....	21
3.2 Methodology.....	21
3.2.1 Attitude and Yaw Kalman Filters.....	22
3.2.2 Lower Body MoCap	23
3.2.3 Ground Contact Measurements.....	25
3.2.4 Robust Kalman Filter	27
3.3 Experimental Setup and Protocol	32
3.3.1 Experimental Setup	32
3.3.2 Experimental Protocol.....	33
3.4 Experimental Results and Discussion.....	35
3.4.1 UWB Estimation Errors.....	35

3.4.2	Parameters.....	36
3.4.3	Robust Filters	38
3.5	Conclusion.....	44
Chapter 4. Conclusion.....		46
4.1.	Thesis Summary and Contributions	46
4.2.	Future Recommendations	47
4.3.	Benefits and Significance	49
References		50
Appendix A.	Kalman Filter.....	54
Appendix B.	Orientation Kalman Filter	56
Appendix C.	Rotation and Homogenous Transformation.....	60
Appendix D.	Ethics Approval.....	61

List of Tables

Table 2.1.	Correlation between BLE Trilateration Error and Residue	17
Table 2.2.	RMSE of the Position Tracking With Three Estimation Modes	19
Table 3.1.	Six Estimation Modes of the Robust KF	37
Table 3.2.	RMSE of the UWB and BM Measurements	43
Table 3.3.	RMSE of the Position Tracking With Six Estimation Modes of the Robust KF	43
Table 3.4.	RMSE of the Position Tracking for Two Activity Types Using Mode 6	44

List of Figures

Figure 2.1.	Trilateration estimation with 3 anchor nodes	9
Figure 2.2.	Proposed trilateration and residue of the i^{th} anchor node	9
Figure 2.3.	Overview of the proposed algorithm, including attitude, yaw, and position KFs and smoother.....	12
Figure 2.4.	(a) Experimental lab setup with the target node, the anchor nodes, and reference cameras and (b) Target node with the CC2540 BLE SoC with the omnidirectional antenna, the MTx sensor, and an optical camera marker.....	14
Figure 2.5.	Test area with BLE anchor nodes and optical cameras.....	14
Figure 2.6.	BLE calibration- logarithmic relationship between received (RX) power and the distance in the horizontal trajectory from 6 cm to 90 cm 15	
Figure 2.7.	(a) Position estimate from the BLE trilateration, the proposed algorithm, and the reference; and (b) residue on the Y -axis	16
Figure 2.8.	Absolute errors of trilateration estimations against the residues on the X - and Y -axes.....	16
Figure 2.9.	(a) Forward and (b) smoothed position estimates from the standard KF, the proposed algorithm, and the reference on the Y -axis	18
Figure 2.10.	Kalman gain of the positional state of the position KF on the standard KF and the proposed algorithm The Kalman gain with the BLE outliers (error > 0.3 m) are shown by the x symbol.	19
Figure 2.11.	Horizontal trajectory of the smoothed estimates from the standard KF, the proposed algorithm, and the reference $t= 78$ to 107.3 s	19
Figure 3.1.	Navigation, body, and sensor frames on the lower body segments, including pelvis, right and left thighs, shanks, and foot during the initialization. The positions of the seven IMUs and one UWB tag are attached the body segments.	22
Figure 3.2.	Overview of the proposed algorithm: (1)-(2) 3D orientations on the seven lower body segment are estimated with the attitude and yaw KF using the inertial and magnetic signals (Section 3.2.1); (3) the lower body motion with respect to the body frame is captured using the 3D orientations on the body segments (Section 3.2.2); (4)-(5) the stance phase is detected using the angular rate energy detector with the IMU at the foot (Section 3.2.3); (6)-(7) the position of the root joint is robustly estimated from the UWB position measurement, the external acceleration from the IMU, and the height and velocity measurements (during a stance phase) using the BM and can be post-processed with the RTS	

	smoother (Section 3.2.4); and (8) the lower body motion with respect to the navigation frame is captured with the forward/smoothed root position (Section 3.2.2).	30
Figure 3.3.	(a) Experimental setup with the test subject, UWB receiver, and optical cameras. The test subject is equipped with the MTx IMUs, the Ubisense UWB slim tag, and optical markers. (b) Test area with the UWB receivers, optical cameras, and the GoPro camera.....	32
Figure 3.4.	Results of the walking experiment: (a) UWB estimation error and (b) sampling period	34
Figure 3.5.	Position estimates from the UWB, Mode 1 (a)-(c), Mode 2 (d)-(f), and Mode 3 (g)-(i), and the reference camera system. The columns are based on the types of the UWB measurement errors. The first, second, and third columns are the UWB's outliers ($t= 36.86, 37.08, \text{ and } 41.83 \text{ s}$), four sequential outliers ($t= 62.26 \text{ to } 62.58 \text{ s}$), and the 1.71 s signal outage ($t= 65.84 \text{ to } 67.55 \text{ s}$), respectively. The UWB outliers are shown by the blue x symbols. Table 3.1 summarizes the criterion for the above three modes.	36
Figure 3.6.	Standard deviation of the UWB measurement noise covariance during (a) the outliers ($t= 36.86, 37.08, \text{ and } 41.83 \text{ s}$) and (b) four sequential outliers ($t= 62.26 \text{ to } 62.58 \text{ s}$) with Mode 2. The outliers are shown by black x symbols.	38
Figure 3.7.	Position estimates from the UWB, Mode 4 (a)-(c), Mode 5 (d)-(f), and Mode 6 (g)-(i), and the reference on the Y-axis. The columns are based on the types of the UWB measurement errors and are explained in the Figure 3.5 description. The UWB outliers are shown by blue x symbols.	39
Figure 3.8.	Standard deviation of the UWB measurement noise covariance with Modes 4 (a), Mode 5 (b), and Mode 6 (c) during the outliers ($t= 36.86, 37.08, \text{ and } 41.83 \text{ s}$). The outliers are shown by black x symbols.....	40
Figure 3.9.	Horizontal trajectories of dynamic motions: (a) single-leg jumping and (b) running motions	41
Figure 3.10.	Position and velocity estimates on (a), (c) X-and (b), (d) Z-axes for double-leg jumping.....	41
Figure 3.11.	Single-leg horizontal jump motion (a)-(d) captured by the GoPro camera and (e)-(h) constructed using the proposed algorithm. The jump cycle is broken into four phases: (a), (e) the start of the jump, (b), (f) the lift-off, and (c), (g) the ground-contact, and (d), (h) the end of jump.	42
Figure A.1.	Overview of the orientation algorithm structure	59

List of Acronyms

AOA	Angle of Arrival
BLE	Bluetooth Low Energy
BM	Biomechanical Model
CKF	Cascaded Kalman Filter
DOP	Dilution of Precision
DWNA	Discrete White Noise Acceleration
GPS	Global Positioning System
IAE	Innovation-Based Adaptive Estimation
IMU	Inertial Measurement Unit
KF	Kalman Filter
MEMS	Microelectromechanical Systems
MMAE	Multiple Model Adaptive Estimation
MoCap	Motion Capture
NIS	Normalized Innovation Squared
NLOS	Non-Line-of-Sight
RMSE	Root-Mean-Squared Error
RSSI	Received Signal Strength Indicator
RTS	Rauch-Tung-Striebel
RX	Receive
TDOA	Time Difference of Arrival
UWB	Ultra-Wideband
Wi-Fi	Wireless Fidelity
ZUPT	Zero Velocity Update Rate

Nomenclature

α	Yaw
β	Pitch
γ	Roll
N	Fixed navigation frame
S	Sensor frame
${}^B_A\mathbf{R}$	Rotation matrix of frame A with respect to frame B
c	Cosine
s	Sine
B	Power offset constant
a	BLE environmental variable
d	Distance between a transmitter and a receiver
α	Random noise
P_r	Receive power
x_{tril}	Trilateration estimation in the X -axis
y_{tril}	Trilateration estimation in the Y -axis
d_i	Distance estimated between a transmitter and i^{th} receiver
\mathbf{r}_i	Residue along X - and Y -axes for each distance d_i
\mathbf{r}	Overall residue
\mathbf{x}_k	State
\mathbf{F}_{k-1}	State transition matrix
\mathbf{G}_{k-1}	Input matrix
u_{k-1}	Input
\mathbf{v}_{k-1}	Process noise vector
w_k	Measurement noise
\mathbf{w}_k	Measurement noise vector
z_k	Measurement
\mathbf{z}_k	Measurement vector
\mathbf{H}_k	Observation matrix
${}^N\mathbf{a}_{k-1}$	External acceleration vector
g	Gravity constant (9.81 m/s ²)

${}^N \mathbf{g}$	Gravity vector
\mathbf{Q}_{k-1}	Process noise covariance matrix
R_k	Measurement noise covariance
\mathbf{R}_k	Measurement noise covariance matrix
σ_v^2	Variance of the process noise
$r_x(k)$	Trilateration residue along the X -axis
${}^B \mathbf{P}_A$	Position vector of origin of frame A with respect to frame B
\mathbf{I}	Identity matrix
${}^B \mathbf{T}_A$	Transformation matrix of frame A with respect to frame B
$\mathbf{z}_G(n)$	Measurement sequence of the angular energy detector
N_G	Window size of the angular energy detector
$\mathbf{y}_G(k)$	Tri-axial gyroscope measurement
γ_G	Detection threshold of the angular energy detector
${}^i \boldsymbol{\omega}_i$	Angular velocity of the body frame i
Δt	Sampling time of the IMU
S_k	Innovation covariance
\mathbf{S}_k	Innovation covariance matrix
M_k^2	Normalized innovation squared
H_0	Null hypothesis test
H_a	Alternative hypothesis test
$\lambda_k(i)$	Scaling factor of the innovation covariance
α	Significance level
m	Dimension of the measurement vector \mathbf{z}_k
$\chi_{\alpha,m}^2$	Quantile set by α and m
σ_{UWB}^2	Variance of the UWB measurement
σ_{height}^2	Variance of the BM height measurement
$\sigma_{velocity}^2$	Variance of the BM velocity measurement
σ_A^2	Variance of the accelerometer measurement
σ_G^2	Variance of the gyroscope measurement
σ_M^2	Variance of the magnetometer measurement
c_A	External acceleration model-related constant
ε_M	Threshold for detecting the magnetic disturbance

a_M Maximum acceleration magnitude

Chapter 1.

Introduction

1.1. Overview

Motion capture (MoCap) is the process of recording the movement of objects or person. The MoCap market is a fast-growing field where its market is expected to reach \$142.5 million by 2020, at the growth rate of 10.12% from 2015 to 2020 [1]. It has been successfully applied in a wide range of applications, such as gaming, filmmaking, human kinetics, and rehabilitation. In filmmaking, *Avatar* won the 2010 Academy Award for *Best Visual Effects* [2]. Realistic character motion was generated not by traditional animation, but by capturing the movements of the actors with the optical tracking system [3]. However, such a system requires many expensive optical cameras and a large contained motion studio environment.

With the advent of the microelectromechanical systems (MEMS) sensor technology, wearable technology is an emergent latest phenomenon that is bringing our daily interaction with technology closer than ever before. For example, the Fitbit wristband uses a triaxial accelerometer to monitor the physical activity of a person, such as number of steps taken and calories burned [4]. With additional inertial sensors, such as triaxial gyroscope and triaxial magnetometer, 3D orientation of the human body segments can also be estimated [5]-[7]. This project utilizes wearable radio and inertial sensors to robustly track and capture the real-time human motion under various dynamic activities. By integrating these sensor modalities, the proposed system addresses the frequently observed outliers from non-light-line-of-sight (NLOS) and multipath effects of the wireless positioning system. The proposed wearable and wireless MoCap is designed to capture realistic human motions in larger indoor and outdoor spaces in more natural settings.

1.2. Literature Survey

As inertial sensors shrink in size and cost, they are increasingly embedded into many consumer goods, opening up a number of new applications [8]. Recently, miniature inertial measurement units (IMUs), consisting of MEMS-based tri-axial accelerometers, gyroscopes, and magnetometers, have been deployed as wearable devices to monitor human motion in an ambulatory fashion [9], [10]. In robotics, for example, a humanoid robot can imitate human walking motion in real-time using wearable IMUs [11].

Existing MoCap systems, such as “gold-standard” optical tracking systems, suffer from marker occlusion problems [12] and are confined to a small restricted area due to their fixed external hardware requirements [13]. The key advantages of IMUs are that they are highly portable, provide measurements at a high update rate, and do not suffer from signal blockage. However, the use of an IMU alone suffers from the position drift that grows exponentially due to the instability of sensor bias [14]. Previously, zero velocity update (ZUPT) with a shoe-mounted IMU has been proposed to correct the velocity error by detecting a ground contact, but the position error still grows based on the total walking distance [15]-[17].

Satellite-based navigation systems, such as the Global Positioning System (GPS), address this issue with its absolute location estimate. However, GPS is not suitable for indoor applications as the signals are attenuated and blocked by the walls of buildings [18]. Radio-based wireless location technologies, such as Wi-Fi, Bluetooth, ultra-wideband (UWB), enable tracking a person in an indoor environment [19]. First, the received signal strength indicator (RSSI) from Bluetooth Low Energy (BLE) can be deployed to estimate a distance of a receiver relative to a transmitter. With the multiple distance measurements from the fixed anchor nodes (i.e. transmitters), a trilateration can be used to estimate the absolute position of the target node (i.e. receiver) [20]. However, the position accuracy suffers from the NLOS and multipath [21]. Second, the UWB uses very short pulses to transmit data using a large bandwidth (from 3.1 to 10.6 GHz), where the directed signal can be distinguished against the reflected signals [19]. As a result, the UWB can achieve a higher position accuracy compared to the narrowband

counterparts, require a very low power to run with a coin cell battery (e.g., over 1 year at 1 Hz), and cover a relatively large area (e.g., about 20 m by 20 m) [22], [23]. The UWB has, therefore, been noted as one of the most promising indoor localization technologies. However, in the presence of a large number of multipath signals, UWB often cannot detect the signals from its direct paths, so the position accuracy frequently suffers from the outliers.

On the other hand, a biomechanical model (BM) fused with IMU measurements can be used to obtain valuable information for motion tracking a human subject. The stance phase is denoted when the foot is in contact with the ground and takes up a significant part in our daily activities [24]. For example, it represents 38.5% and 16.8% of the gait cycle for walking and running, respectively [25]. With the ZUPT, a root joint (e.g. waist) can be tracked by propagating the velocity from the foot with the aid of a biomechanical model [15], [24]. The height of the root joint can also be estimated with a BM, but this has not been explored yet in the literature for motion tracking purposes.

Kalman filtering is a widely used technique for state estimation from the multiple sensor measurements [26], [27]. A Kalman filter (KF) makes a key assumption that both process and measurement noises are normally distributed [28]. However, the measurement noises of the wireless positioning systems do not satisfy this assumption very well due to frequent heavy-tailed outliers [29], [30]. To address this issue, researchers have introduced adaptive KFs, such as multiple model adaptive estimation (MMAE) and innovation-based adaptive estimation (IAE). The MMAE estimates the states by running multiple KFs with different state-space models and process and measurement noise covariances [26], [31]. However, there is a high computational cost of running the multiple KFs in parallel and can limit real-time applications. In the IAE, new process and/or measurement noise covariances are adapted based on the window-based innovation sequence, but the state estimates can often diverge [32].

1.3. Objective

The overall objective of this research is to develop a robust tracking and motion capture of human/sensor using wireless positioning systems (UWB/BLE) and IMU. Key technical considerations involved in the research are: (i) wearable technology, (ii) motion capture, (iii) sensor fusion, and (iv) sensor noise.

Wearable Technology

As the inertial and radio sensors are becoming more miniature and powerful, they are widely deployed as wearable sensors bringing our daily interaction with technology closer than before. They should be portable and unobtrusive, and the sensor measurements should be accessible with software in real-time. They should provide useful measurements that can be used for many practical applications.

Motion Capture

Human motion should be able to be accurately captured in a large space. A high update rate ($> 60\text{Hz}$) is especially applicable to capture the high-speed activities involving rapid directional changes. It should not suffer from growing positioning errors, outliers, and signal outage. A low cost will be advantageous for many practical applications. A low computational cost may be desired for real-time purposes.

Sensor Fusion

Sensor fusion is a method of integrating measurements from multiple sensors, such as the IMU, consisting of 3-axis accelerometer, 3-axis rate gyros, and 3-axis magnetometer, and a radio-based wireless positioning system (e.g., UWB or BLE). Each sensor may exhibit different update rate and accuracy. The goal of the sensor fusion is to improve the performance of the state (position and velocity) estimation by employing multiple sensors compared to the use of a single sensor.

Sensor Noise

Inertial and radio sensors exhibit different behaviors. The accelerometer and gyroscope in the IMU are commonly modelled with a zero-mean Gaussian distribution where its standard deviation is obtained by the sensor lying still on the floor. On the other hand, the radio-based wireless positioning systems (e.g., UWB or BLE) suffer from the frequent outliers from the NLOS and multipath, so they cannot be well modelled with a standard Gaussian distribution. Understanding these sensor behaviors is important for estimating the desired states with the sensor fusion.

1.4. Contributions

First, a novel three-step cascaded Kalman filter (CKF) is proposed to accurately estimate the sensor position in the presence of the outliers. The position is estimated by fusing the external acceleration from the IMU and the trilateration estimation from the BLE. Using the estimated roll, pitch, and yaw, the acceleration measurements are rotated from the moving sensor to the fixed navigation frames. The weight of the trilateration estimation is adaptively set based on the residue between the distance measurements and the trilateration estimation. The position accuracy is further improved with the Rauch-Tung-Striebel (RTS) smoother. The experimental results show that the residue has a strong correlation with the trilateration estimation error, and the proposed algorithm can estimate the position more robustly compared to the standard KF in the face of outliers.

Second, a drift-free and real-time motion tracking algorithm is presented by integrating the IMU and UWB signals and domain-specific sensor fusion that takes advantage of more accurate 3D velocity and height information obtained with the aid of a BM. In the literature, the motion tracking algorithms are mainly based on the following approaches: (i) sensor fusion of the IMU and an absolute positioning system (e.g., UWB) [6] or (ii) the ZUPT [15]. To the best of authors' knowledge, there has not been work that fuses the measurements from all of these sensor modalities. Compared to the UWB, the proposed algorithm uses the IMU's high update rate to capture high-speed activities

involving rapid directional changes. During the UWB signal outage, the algorithm makes use of the IMU-aided BM instead of double integrating the IMU acceleration. Prior to sensor data fusion using the sequential KF, the normalized innovation squared (NIS) test is deployed to detect and weight the outliers by rescaling the measurement noise covariance. The novelty of the proposed algorithm is that it can maintain high accuracy and robustness on motion trajectory tracking and MoCap under various dynamic activities, such as walking, running, and jumping. The algorithm has been experimentally verified for real-world activities, where the radio positioning systems such as UWB frequently suffer from outliers and signal outages.

1.5. Thesis Outline

This thesis is divided into the following chapters. In Chapter 2, the above adaptive KF for indoor localization using the BLE and IMU is presented, which has been published in [33]. Chapter 3 presents the above robust biomechanical model-based motion tracking algorithm for the lower body using the UWB and IMU, which has been disseminated to [34]. Chapter 4 concludes my thesis and provides suggestions for future research.

Chapter 2.

Adaptive Kalman Filter for Indoor Localization Using BLE and IMU

2.1 Introduction

This chapter presents an adaptive sensor fusion algorithm to accurately track the 2D location of the sensor using the BLE and IMU. The omnidirectional BLE antennas are deployed to verify the performance of the proposed algorithm in the 2D trajectory instead of the 3D. The reason is that they equally radiate the signal only in all horizontal directions. They are different from isotropic antennas which radiate equal power in all directions and exist only in theory. Section 2.2 shows a three-step CKF to track the sensor in the presence of the outliers. The experimental setup and protocol is explained in Section 2.3. The experimental results on tracking 2D trajectory of the sensor are discussed in Section 2.4. This chapter concludes in Section 2.5 with a brief summary of the main findings.

2.2 Methodology

This section explains the theory behind the proposed 2D indoor localization algorithm. The method of estimating the 3D orientation of the moving node using the IMU is presented in Section 2.2.1. In Section 2.2.2, 2D absolute position of the moving node is estimated using the trilateration which takes the RSSI measurements from multiple BLE anchor nodes as inputs. Section 2.2.3 describes how to robustly track the location of the moving node using available sensor measurements.

2.2.1 Attitude and Yaw Kalman Filters

This work employs the previously proposed attitude and yaw KFs (Appendix B) to estimate the α (yaw), β (pitch), and γ (roll), which represent the rotation angles about the Z -, Y -, and X -axes of the fixed navigation frame N , respectively. The algorithms are described in [5] and [28].

The state of the attitude KF is set as the last row of the rotation matrix ${}^N_S\mathbf{R}$ of the sensor frame S with respect to the navigation frame N expressed as following:

$${}^N_S\mathbf{R} = \begin{bmatrix} cac\beta & cas\beta s\gamma - sac\gamma & cas\beta c\gamma + sas\gamma \\ sac\beta & sas\beta s\gamma + cac\gamma & sas\beta c\gamma - cas\gamma \\ -s\beta & c\beta s\gamma & c\beta c\gamma \end{bmatrix} \quad (2.1)$$

where c and s are abbreviation for cosine and sine respectively. The states are first estimated with triaxial accelerometer and gyroscope measurements. β and γ are calculated with the states [28].

The states of the yaw KF are set as the first row of ${}^N_S\mathbf{R}$, which are calculated using triaxial gyroscope and magnetometer measurements along with the estimated β and γ from the attitude KF. α is estimated from β and γ and the states [5].

2.2.2 Trilateration

By assuming that the receivers and transmitters have omnidirectional antennas and the transmitter has a constant transmit power, the receive power P_r (i.e. RSSI) on the receiver can be determined by [21]

$$P_r = B - a \log_{10} d + \alpha \quad (2.2)$$

where B is the power offset constant; a is the environmental variable; d is the distance between a transmitter and a receiver; and α is the random noise. For the fixed environment, a is set as a constant. d is estimated from P_r , a , and B by

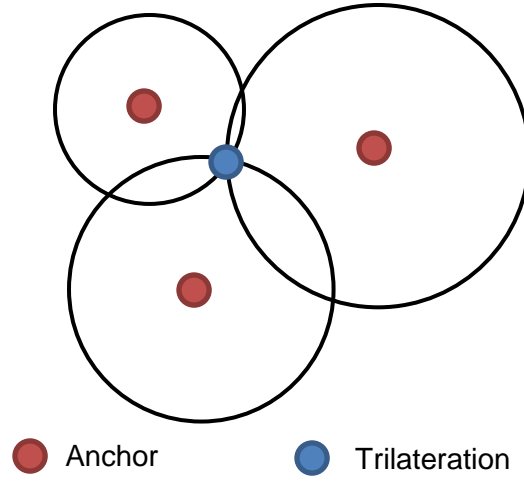


Figure 2.1. Trilateration estimation with 3 anchor nodes

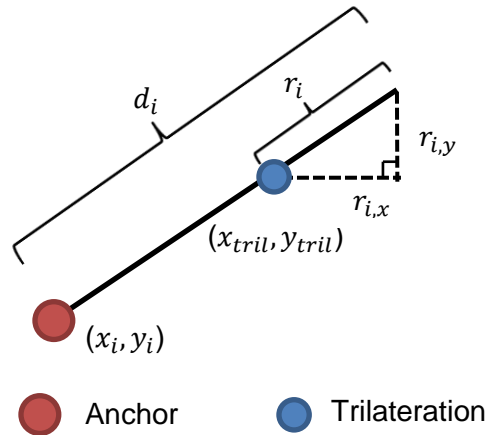


Figure 2.2. Proposed trilateration and residue of the i^{th} anchor node

$$d = 10^{P_r - B/a}. \quad (2.3)$$

The trilateration is deployed to estimate the position of the target node $\hat{\mathbf{x}}$ ($= [x_{tril} \ y_{tril}]^T$) [20]. Based on the estimated distances d_i and the known positions (x_i, y_i) of n anchor nodes, the position $\hat{\mathbf{x}}$ is expressed in the form of $\mathbf{A}\hat{\mathbf{x}} = \mathbf{b}$ and solved as the least-squares problem, i.e. $\hat{\mathbf{x}} = (\mathbf{A}^T \mathbf{A})^{-1} \mathbf{A}^T \mathbf{b}$ (Figure 2.1):

$$\mathbf{A} = \begin{bmatrix} 2(x_1 - x_n) & 2(y_1 - y_n) \\ \vdots & \vdots \\ 2(x_{n-1} - x_n) & 2(y_{n-1} - y_n) \end{bmatrix} \quad (2.4)$$

$$\mathbf{b} = \begin{bmatrix} x_1^2 - x_n^2 + y_1^2 - y_n^2 + d_n^2 - d_1^2 \\ \vdots \\ x_{n-1}^2 - x_n^2 + y_{n-1}^2 - y_n^2 + d_n^2 - d_{n-1}^2 \end{bmatrix}. \quad (2.5)$$

The sanity check of the trilateration estimation $\hat{\mathbf{x}}$ can be done by computing the residue between the estimated distance d_i and the distance to the location estimate $\hat{\mathbf{x}}$ is calculated as following (Figure 2.2) [20]:

$$r_i = \left| \sqrt{(x_i - x_{tril})^2 + (y_i - y_{tril})^2} - d_i \right|. \quad (2.6)$$

The previous work simply rejected the estimated location $\hat{\mathbf{x}}$ when the residue is larger than the threshold value [20]. This section proposes estimating the residue \mathbf{r}_i ($= [r_{i,x} \ r_{i,y}]^T$) along X - and Y -axes for each distance d_i which is determined by (2.7) and (2.8) in a sequence (Figure 2.2). The residue \mathbf{r}_i is used to adaptively weight the BLE trilateration estimation on X - and Y -axes for estimating the 2D position of the target node (Section 2.2.3).

$$\mathbf{r}_i = [|x_i - x_{tril}| \ |y_i - y_{tril}|]^T \quad (2.7)$$

$$\mathbf{r}_i = r_i \frac{\mathbf{r}_i}{\|\mathbf{r}_i\|} \quad (2.8)$$

The overall residue \mathbf{r}_i ($= [r_x \ r_y]^T$) along X - and Y -axes is averaged over the multiple residues \mathbf{r}_i as follows:

$$\mathbf{r}_i = \frac{1}{n} \left[\sum_{i=1}^n r_{i,x} \quad \sum_{i=1}^n r_{i,y} \right]^T. \quad (2.9)$$

2.2.3 Position Kalman Filter

In the position KF, the 2D position of the target node is estimated with the external acceleration from the IMU and the trilateration estimation. The states are the 2D position and velocity of the target node. As the states of each axis are independent of each other, the states $\mathbf{x}_k (= [x_k \ \dot{x}_k]^T)$ are set for each axis, where x_k and \dot{x}_k are the position and velocity, respectively. This section only considers capturing the states in the X -axis, and the states of the other axes can similarly be estimated. The KF is governed by following linear discrete-time equations:

$$\mathbf{x}_k = \mathbf{F}_{k-1}\mathbf{x}_{k-1} + \mathbf{G}_{k-1}u_{k-1} + \mathbf{v}_{k-1} \quad (2.10)$$

$$z_k = \mathbf{H}_k\mathbf{x}_k + w_k \quad (2.11)$$

where \mathbf{F}_{k-1} and \mathbf{G}_{k-1} are the state transition and input matrices; u_{k-1} is the input; \mathbf{v}_{k-1} and w_k are the process noise vector and the measurement noise; z_k is the measurement; and \mathbf{H}_k is the observation matrix. The model is set as the discrete white noise acceleration (DWNA) where the variables are defined as follows [26]:

$$\mathbf{F}_{k-1} = \begin{bmatrix} 1 & \Delta t \\ 0 & 1 \end{bmatrix} \quad (2.12)$$

$$\mathbf{G}_{k-1} = [\Delta t^2/2 \ \Delta t]^T \quad (2.13)$$

$$u_{k-1} = {}^N a_{k-1} \quad (2.14)$$

$$\mathbf{H}_k = [1 \ 0] \quad (2.15)$$

$$z_k = x_{tril}(k) \quad (2.16)$$

where Δt is the sampling period of the IMU, and ${}^N a_{k-1}$ is the first component of the external acceleration vector corresponding to X -axis, ${}^N \mathbf{a}_{k-1} (= {}^N_s \mathbf{R}_{k-1} {}^s \mathbf{a}_{k-1} - {}^N \mathbf{g})$. ${}^N \mathbf{g}$ ($= [0 \ 0 \ g]^T$) is the gravity vector in the navigation frame where g is 9.81 m/s^2 . $x_{tril}(k)$

is the BLE trilateration estimation on the X -axis using (2.4), (2.5). \mathbf{Q}_{k-1} and R_k are the process and measurement noise covariances with following characteristics:

$$\mathbf{Q}_{k-1} = \begin{bmatrix} \Delta t^4/4 & \Delta t^3/2 \\ \Delta t^3/2 & \Delta t^2 \end{bmatrix} \sigma_v^2 \quad (2.17)$$

$$R_k = r_x^2(k) \quad (2.18)$$

where σ_v^2 is the variance of the process noise, and $r_x^2(k)$ is the trilateration residue along the X -axis (2.9). With the variables defined as above, the procedure for estimating the states are found in Appendix A.

In the applications where real-time data processing is not required, the RTS smoother (Appendix A) can be deployed to improve the accuracy of the forward state estimate from the position KF [26], [27]. The smoother is consisted of forward and backward filters. The forward filter estimates the forward states and covariances using the position KF (2.10), (2.11). Then, the backward filter estimates the smoothed states and covariances in a backward sweep from the end of data to the beginning.

The overview structure of the proposed algorithm is shown in Figure 2.3.

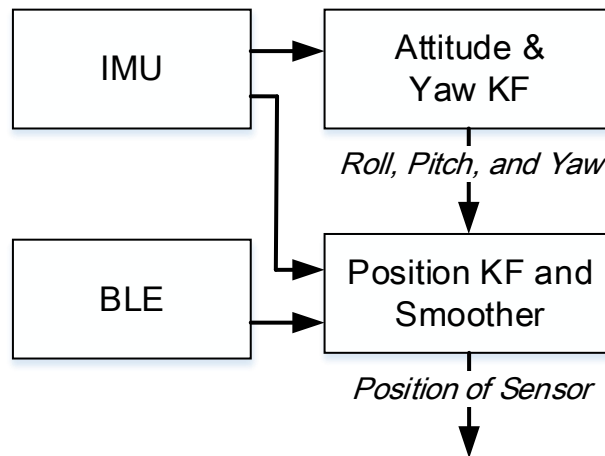


Figure 2.3. Overview of the proposed algorithm, including attitude, yaw, and position KFs and smoother

2.3 Experimental Setup and Protocol

2.3.1 Experimental Setup

The performance of the proposed algorithm was tested in an indoor space. As shown in Figure 2.4(a) and Figure 2.5, three anchor nodes were placed close to the outside line of the test area. Both target and anchor nodes were equipped with the CC2240 BLE system-on-chip (SoC) (from Texas Instruments) connected to the omnidirectional ANT-DB1-RAF antenna (from Linx Technologies). The transmit power of the anchor nodes was set at -23 dBm. The target node received the RSSI from each transmitter at different times with a sampling rate of about 80Hz. The RSSIs from each transmitter were averaged at 10Hz when using the trilateration. The target node was additionally equipped with the MTx IMU (from Xsens Technologies) at the sampling rate of 100Hz. The Qualisys optical tracking system was used as a reference system at the sampling rate of 100Hz. Eight optical cameras were placed around the test area (Figure 2.4(a) and Figure 2.5). Figure 2.4(b) shows the target node with the BLE SoC with the omnidirectional antenna, the IMU, and an optical marker.

Prior to the experiments, the RSSI measurement were collected to best fitted to calculate the parameters α and B in (2.3) for each anchor node. the target node moved away from each anchor node from 6 cm to 90 cm. The distance was 6 to 10 cm with an increment of 2 cm and 15 cm to 85 cm with an increment of 5 cm. The data was collected for 5 s and was repeated 3 times. Figure 2.6 shows the received power and the best-fit logarithmic curve of the RSSI measurements for one of the anchor node. For this anchor node, α and B were set to -21.99 and -26.55 . These parameters were kept the same because the test environment was constant throughout the experiments. However, the power attenuation relationship with the distance (2.3) may not be stationary after a long usage of the BLE systems. The reason is that the battery drain can potentially decrease the BLE transmit power. Therefore, it is recommended to verify these variables after a long period of experiments in the future.

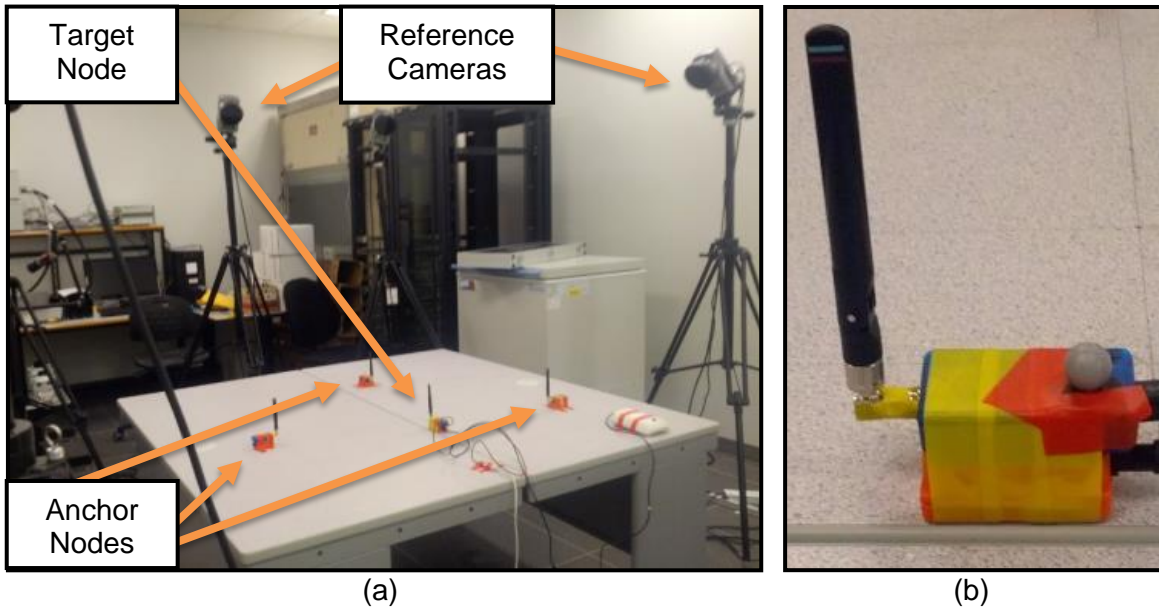


Figure 2.4. (a) Experimental lab setup with the target node, the anchor nodes, and reference cameras and (b) Target node with the CC2540 BLE SoC with the omnidirectional antenna, the MTx sensor, and an optical camera marker

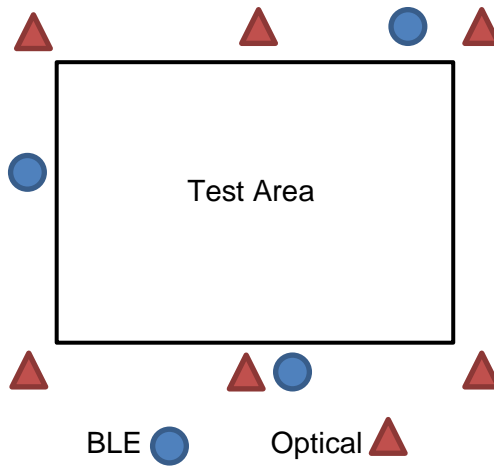


Figure 2.5. Test area with BLE anchor nodes and optical cameras

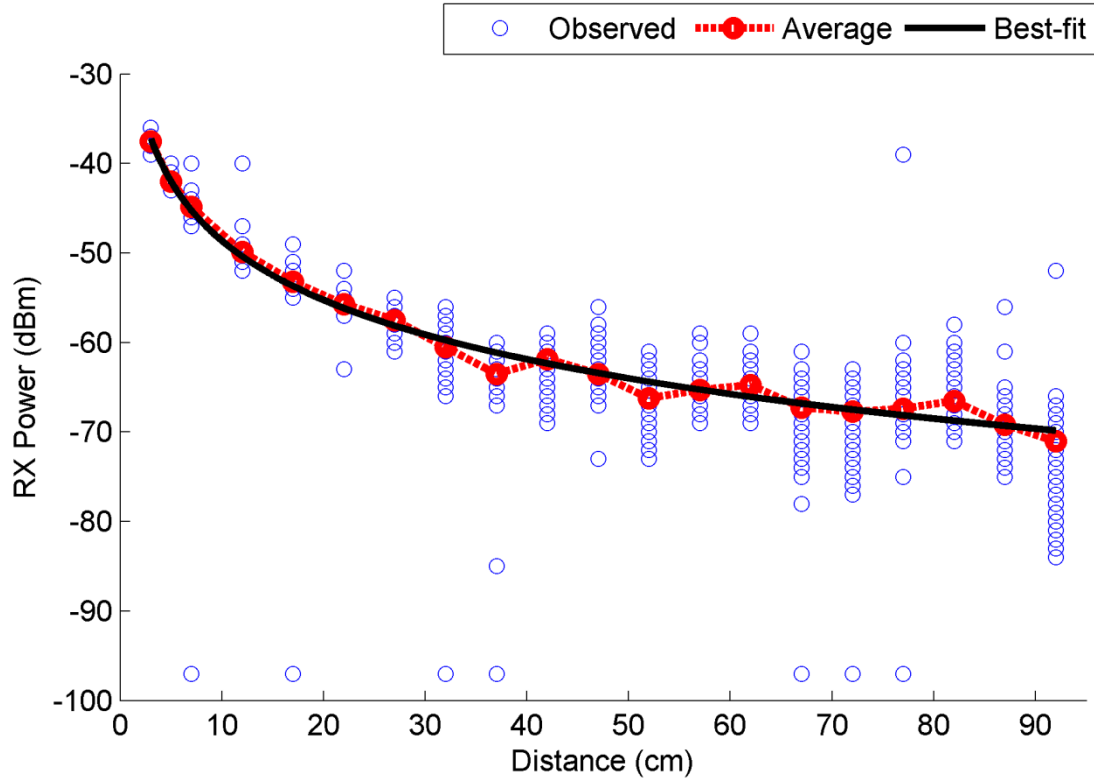


Figure 2.6. BLE calibration- logarithmic relationship between received (RX) power and the distance in the horizontal trajectory from 6 cm to 90 cm

2.3.2 Experimental Protocol

In each experimental trial, the target node was continuously moved in the rectangular trajectories of 70 cm by 80 cm in about 60 s. The test was repeated for 10 times. The parameters of the proposed algorithm were estimated by the inertial measurements with the stationary IMU. The accelerometer noise variance σ_A^2 , the gyroscope noise variance σ_G^2 , and the magnetometer noise variance σ_M^2 were calculated as $10^{-4} \text{ m}^2/\text{s}^4$, $4 \times 10^{-5} \text{ rad}^2/\text{s}^2$, and $2 \times 10^{-3} \text{ mT}^2$, respectively. The external acceleration model-related constant c_A was set to 0.1 which provides a good result for estimating the attitude angles under various dynamic conditions [28]. σ_v^2 was set at $1 \text{ m}^2/\text{s}^4$ based on a range of maximum acceleration magnitude a_M as $0.5a_M \leq \sigma_v \leq a_M$.

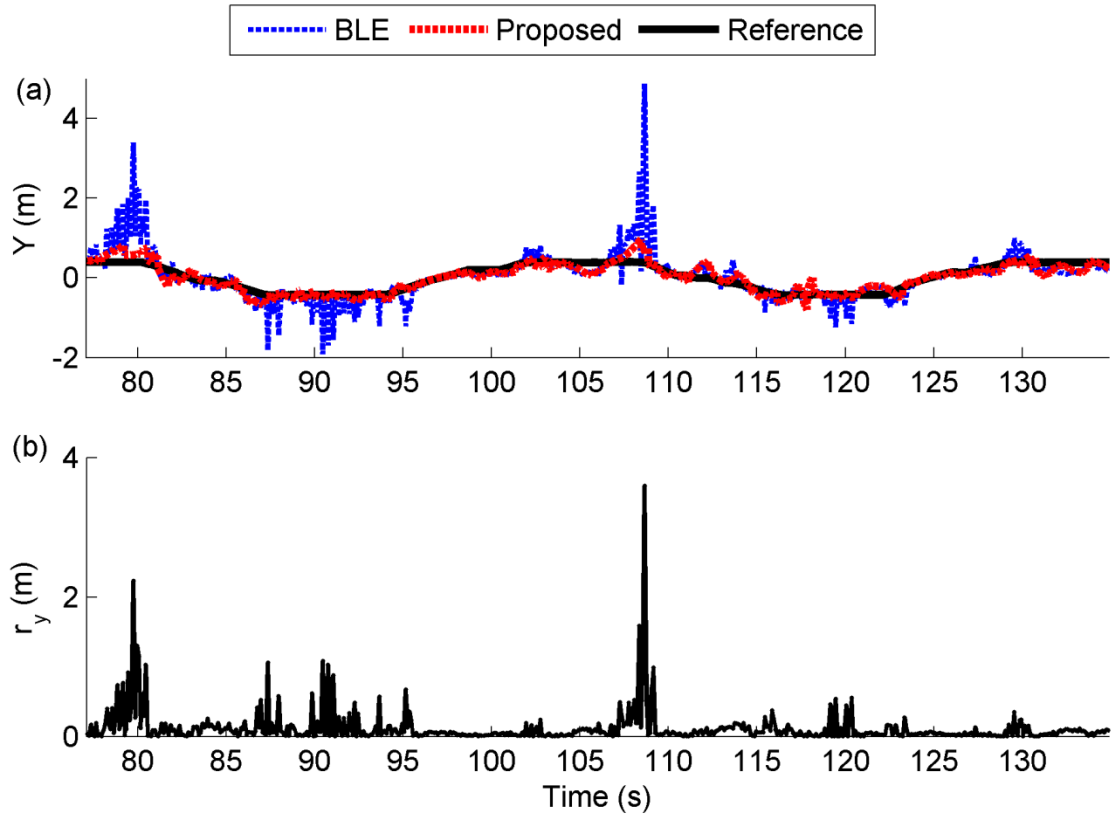


Figure 2.7. (a) Position estimate from the BLE trilateration, the proposed algorithm, and the reference; and (b) residue on the Y-axis

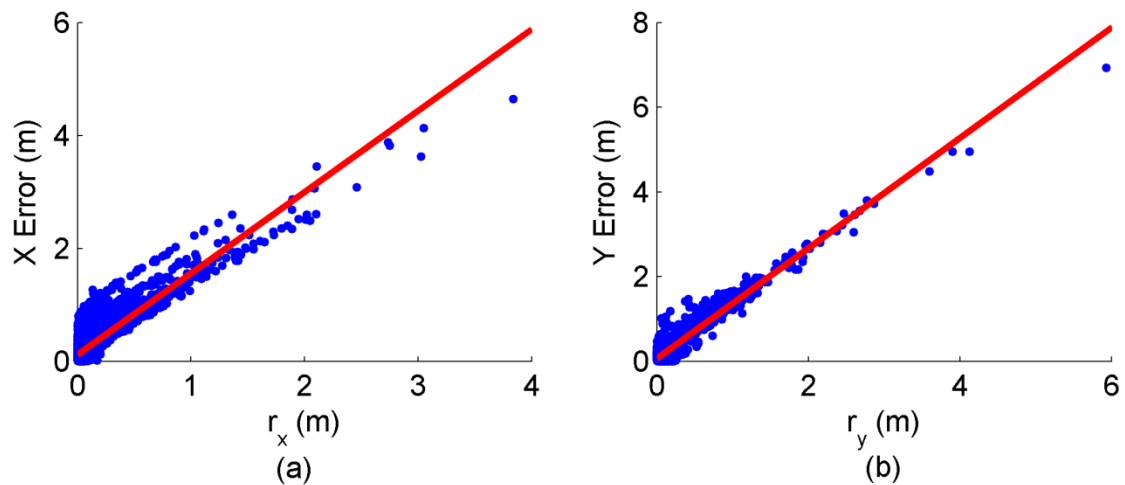


Figure 2.8. Absolute errors of trilateration estimations against the residues on the X- and Y-axes

Table 2.1. Correlation between BLE Trilateration Error and Residue

BLE Trilateration Error	Residue	Correlation
X	X	0.889
	2D	0.864
Y	Y	0.938
	2D	0.829

2.4 Experimental Results and Discussion

Figure 2.7 compares the trilateration estimation against the proposed algorithm on the Y -axis. Figure 2.7(a) shows that the proposed algorithm is robust against the outliers from the trilateration. The residue maintains a strong correlation with the absolute error of trilateration estimation throughout the experiment (Figure 2.7(b)). The maximum trilateration error is 4.49 m at 108.65 s, where the residue is 3.60 m. Figure 2.8 shows the residues against the trilateration errors for all 10 tests. The correlations of 0.889 and 0.938 on the X - and Y -axes suggest that the residue can provide the estimate to the reliability of the trilateration estimation well (Table 2.1). The residues r_i on the X - and Y -axes are more correlated to the BLE errors compared to 2D residue r_i (by an average of 0.067) (Table 2.1).

Next, the performance of the proposed algorithm is compared against that of a standard KF on the Y -axis. The standard KF assumes a constant trilateration measurement noise. The measurement noise covariance R_k along the X - and Y -axes are tuned as 10^{-2} m^2 . The standard KF produces a large root-mean-squared error (RMSE) of 0.935m from $t=79$ to 82 s (Figure 2.9(a)). The proposed algorithm, on the other hand, rejects the outliers and accurately tracks the position with a RMSE of 0.255 m during this time interval. Most of the trilateration estimation from $t=78$ to 80 s deviate from the reference trajectory, resulting in an RMSE of 1.073 m (Figure 2.7(a)). The proposed algorithm has a lower average Kalman gain of 0.033 during the BLE outliers (error > 0.3 m) compared to the standard KF with an average Kalman gain of 0.224 (Figure 2.10). The smaller Kalman gain of the proposed algorithm indicates that a greater weight is put to the IMU measurements compared to the trilateration during the

BLE outliers. The Kalman gain is reduced due to the large estimated residue during this time period (Figure 2.7(b)). With the RTS smoother, Figure 2.9(b) and Figure 2.11 show that the positioning performance is further improved. However, the small drift on the standard KF is still present from $t = 78$ to 80 s (Figure 2.9).

Table 2.2 compares the RMSE in position tracking using the BLE trilateration, the standard KF, and proposed algorithm for all tests. For the real-time estimates, the 2D position accuracy of the proposed algorithm is improved by 54.7% and 44.2% compared to the BLE trilateration and the standard KF, respectively. With the smoother, its 2D positioning accuracy is further improved by 37.1% and 28.3% compared to the standard KF with the smoother and the proposed algorithm without the smoother, respectively.

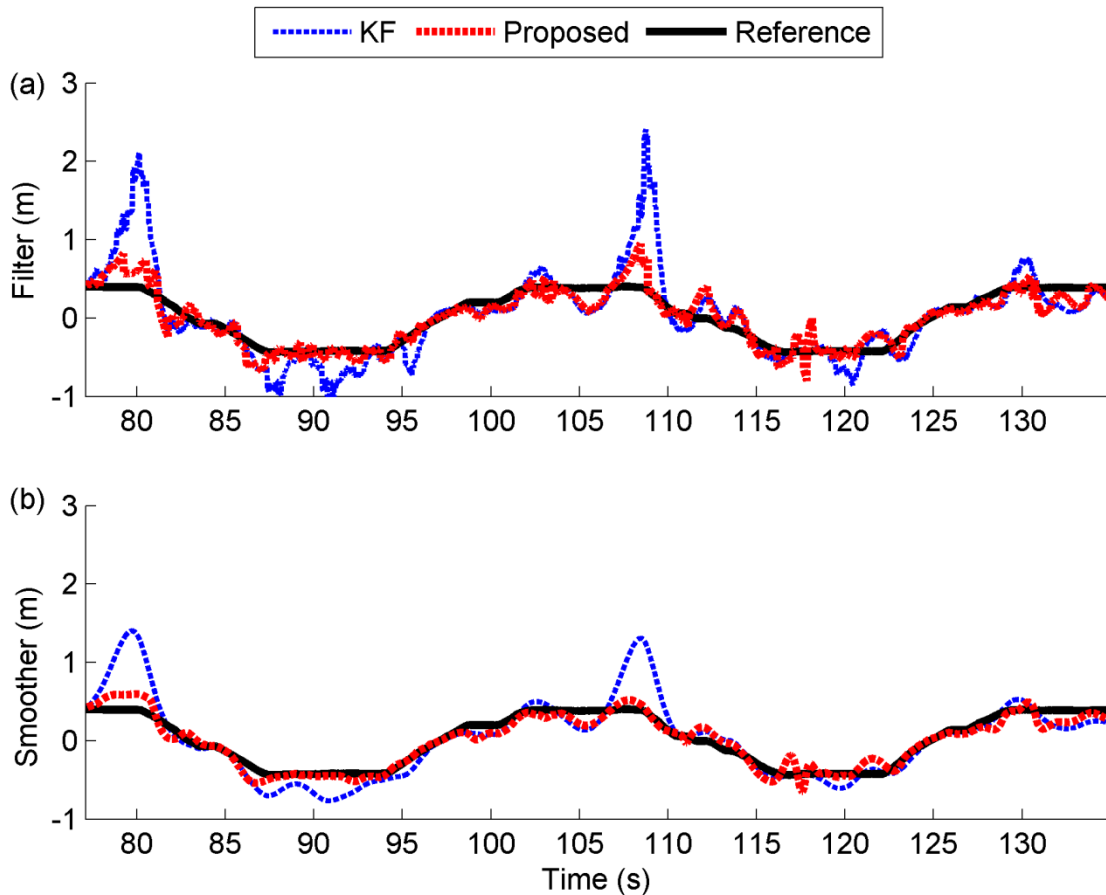


Figure 2.9. (a) Forward and (b) smoothed position estimates from the standard KF, the proposed algorithm, and the reference on the Y -axis

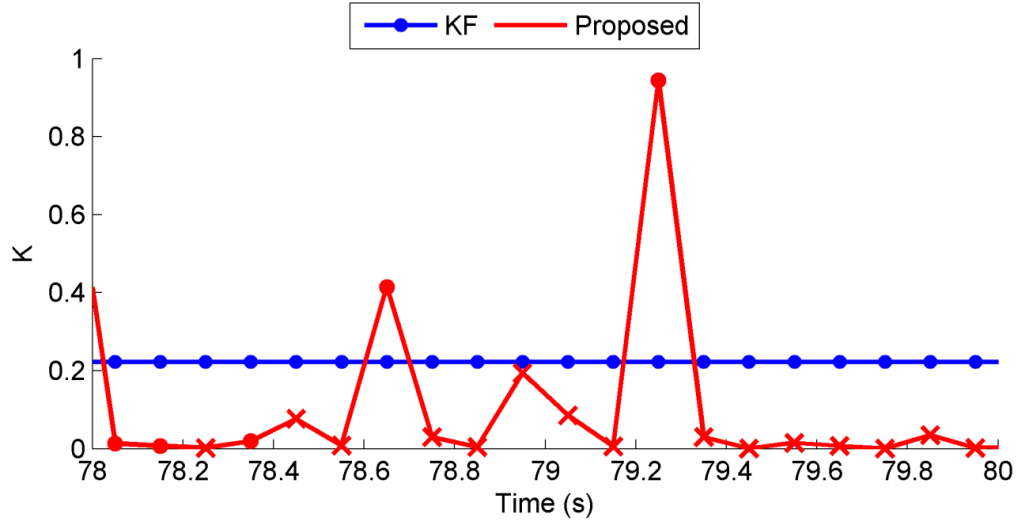


Figure 2.10. Kalman gain of the positional state of the position KF on the standard KF and the proposed algorithm. The Kalman gain with the BLE outliers (error > 0.3 m) are shown by the x symbol.

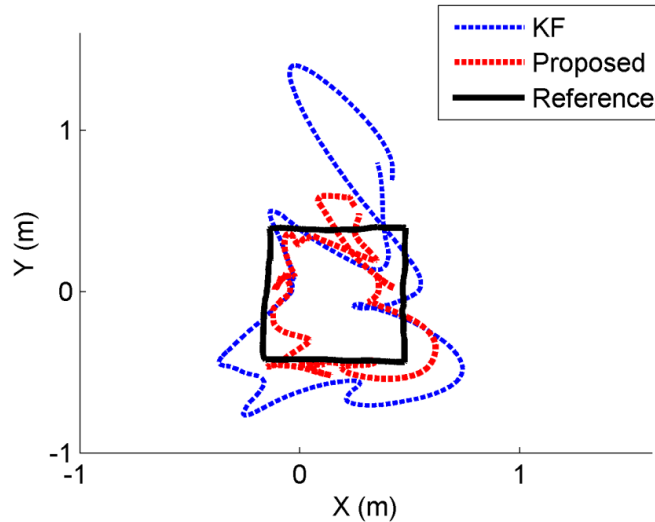


Figure 2.11. Horizontal trajectory of the smoothed estimates from the standard KF, the proposed algorithm, and the reference $t = 78$ to 107.3 s

Table 2.2. RMSE of the Position Tracking With Three Estimation Modes

Modes	Forward (cm)			Smoothing (cm)		
	X	Y	2D	X	Y	2D
BLE	44.1	42.5	61.3	-	-	-
Standard KF	34.0	36.4	49.8	20.3	24.2	31.6
Proposed	21.8	17.2	27.8	16.4	11.3	19.9

2.5 Conclusion

In this chapter, a novel three-step cascaded Kalman filter for accurate estimation of the position trajectories with the IMU and BLE trilateration measurement is proposed. Based on the strong correlation between the trilateration residue and trilateration error, the proposed algorithm uses the residue to adaptively weight the trilateration estimate and the external acceleration, thus the algorithm not requiring manual tuning of the filter parameters. The experimental results have shown that the proposed algorithm can accurately track the moving sensor in the presence of the outliers, and the accuracy is further improved by post-processing using the RTS smoother.

Chapter 3.

Robust Biomechanical Model-based Motion Tracking of Lower Body Using UWB and IMU

3.1 Introduction

The narrowband radio technology (BLE) is more prone to the multipath and NLOS compared to the UWB system [19]. As a result, it may not be able to accurately track the human motion under dynamic activities in a larger space (e.g., over 2 m by 2 m). This chapter shows how to accurately track the location and capture the lower body motion using the UWB and IMU. Section 3.2 shows how to systematically construct a lower body motion using the IMUs and UWB sensor attached on the body segments. The robust trajectory algorithm is also explained in this section. The experimental setup and protocol of slow (walking) and dynamic (running and jumping) activities are explained in Section 3.3. The experimental results on tracking 3D trajectory of a subject for these activities are discussed in Section 3.4. This chapter concludes in Section 3.5 with a brief summary of the main findings.

3.2 Methodology

This section explains the theory behind the proposed 3D orientation estimation and lower body MoCap. The method of estimating the 3D orientation of the body segments using the IMUs is presented in Section 3.2.1. The lower body motion is then systematically constructed with the estimated orientations in Section 3.2.2. In Section 3.2.3, the velocity and height of the root joint (waist) are estimated from the BM during the stance phase. Section 3.2.4 describes how to robustly track the location of a human subject using the available sensor measurements.

3.2.1 Attitude and Yaw Kalman Filters

This section employs the previously proposed cascaded attitude and yaw KFs (Appendix B) to estimate the α (yaw), β (pitch), and γ (roll), which are the orientation about the Z -, Y -, and X -axes of the navigation frame N , respectively [5], [28].

The state of the attitude KF is set as the last row of the rotation matrix ${}^N_S\mathbf{R}$ of the sensor frame S with respect to N expressed as following:

$${}^N_S\mathbf{R} = \begin{bmatrix} cac\beta & cas\beta s\gamma - sac\gamma & cas\beta c\gamma + sas\gamma \\ sac\beta & sas\beta s\gamma + cac\gamma & sas\beta c\gamma - cas\gamma \\ -s\beta & c\beta s\gamma & c\beta c\gamma \end{bmatrix} \quad (3.1)$$

where c and s are abbreviation for cosine and sine, respectively. The states are first estimated with the tri-axial accelerometer and gyroscope measurements. β and γ are calculated from the states [28].

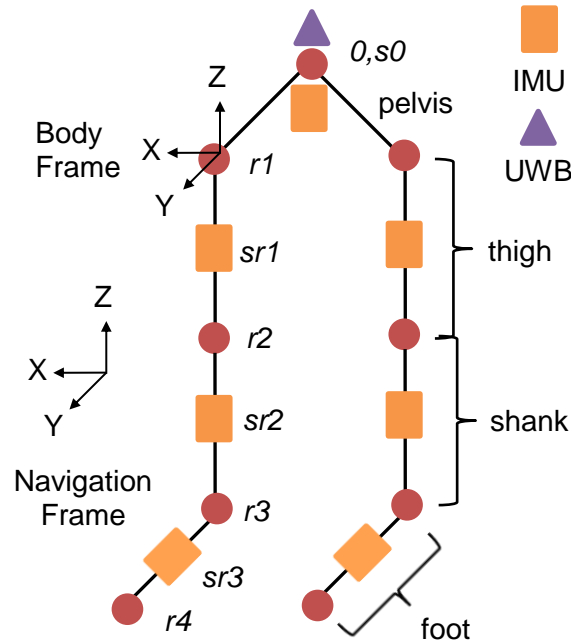


Figure 3.1. Navigation, body, and sensor frames on the lower body segments, including pelvis, right and left thighs, shanks, and foot during the initialization. The positions of the seven IMUs and one UWB tag are attached the body segments.

The yaw KF calculates the yaw α by setting its states as the first row of ${}^N_S\mathbf{R}$, which are estimated with the tri-axial gyroscope and magnetometer measurements and the estimated attitude (i.e. β and γ) from the attitude KF [5], [7]. This yaw KF has the advantage of detecting magnetic disturbances to bridge the temporary disturbances (less than about 20 s long) that frequently happen in an indoor environment [5].

As shown in Figure 3.1, the orientation filters in this section employs the inertial and magnetic data from the seven IMUs attached to the seven major lower body segments including the pelvis, thighs, shanks and the feet; and output the 3D orientation of the body segments in the navigation frame for lower body MoCap purposes (Section 3.2.2).

3.2.2 Lower Body MoCap

This section provides a systematic method for capturing the lower body motion using the IMUs. Three different types of frames, including navigation N , body, and sensor, are used to represent the motion of the body segments. The navigation frame is fixed to the Earth's ground. The body and sensor frames are fixed to the body segments and the IMUs, respectively. The body segment frame indexes are 0, 1, 2, 3, and 4, which are located on the upper end joint of the body segments including the waist, thigh, shank, foot, and toe, respectively. Similarly, the corresponding sensor frames of the IMUs attached to the body segments are denoted by $s0$, $s1$, $s2$, $s3$, and $s4$. The indexes of the right and left legs are denoted by r and l . For example, $r2$ represents the body frame of the right shank and $sl3$ represents the sensor frame of the left foot. The dominant motion of the knee is flexion and extension, and its corresponding axis is denoted by the X -axis of the body frames. The directions and locations of the navigation, body and sensor frames are shown in the Figure 3.1. We assume that the body segments are rigid, where the dimensions of the body segments are constant throughout the experiments [24], [35]. Herein, only the method of capturing the right leg motion is explained, and the left leg can similarly be captured as the right leg.

Prior to the experiments, the dimensions of the body segments are measured. Using these measurements, the position vectors between the origins of the body frames

are formed as: ${}^0\mathbf{P}_{r1}$, ${}^{r1}\mathbf{P}_{r2}$, ${}^{r2}\mathbf{P}_{r3}$, and ${}^{r3}\mathbf{P}_{r4}$ (Figure 3.1). For instance, ${}^{r1}\mathbf{P}_{r2}$ is the origin of the shank body frame with respect to the thigh body frame. Additionally, the rotation matrices between the body and sensor frames are calculated. To this end, the test subject is also asked to stand in a way that the body frames are aligned to the navigation frame (Figure 3.1). Thus, the rotation matrix from the navigation frame to each body frame is an identity matrix (i.e. ${}^0\mathbf{R} = \mathbf{I}$). The rotation matrix of each sensor frame with respect to its body frame (i.e. ${}_{s0}^0\mathbf{R}$) is calculated as follows:

$${}_{s0}^0\mathbf{R} = {}^0\mathbf{R}_N {}^N\mathbf{R}_{s0} = \mathbf{I}_N {}^N\mathbf{R}_{s0} = {}^N\mathbf{R}_{s0} \quad (3.2)$$

where ${}^N\mathbf{R}_{s0}$ is the estimated rotation matrix using the attitude and yaw KFs (Section 3.2.1).

The lower body motion is constructed with the positions of the body frames (${}^N\mathbf{P}_{r1}$, ${}^N\mathbf{P}_{r2}$, ${}^N\mathbf{P}_{r3}$, and ${}^N\mathbf{P}_{r4}$), which results in two kinematic chains with a pelvis body frame as a base (Figure 3.1). The procedure of obtaining these positions deploys the rotation and homogenous transformation (Appendix C) and is summarized below.

- 1) Estimate the 3D orientations of the IMUs on the body segments (${}_{s0}^N\mathbf{R}, \dots, {}_{sr3}^N\mathbf{R}$) (Section 3.2.1).
- 2) Formulate the rotation matrices between neighboring sensor frames (${}_{sr1}^{s0}\mathbf{R}, \dots, {}_{sr3}^{sr2}\mathbf{R}$), i.e.

$${}_{sr1}^{s0}\mathbf{R} = {}^N\mathbf{R}_{s0}^T {}^N\mathbf{R}_{sr1} \quad (3.3)$$

- 3) Convert to the rotation matrices between neighboring body frames (${}_{r1}^0\mathbf{R}, \dots, {}_{r4}^{r3}\mathbf{R}$), i.e.

$${}_{r1}^0\mathbf{R} = {}^0\mathbf{R}_{s0} {}_{sr1}^{s0}\mathbf{R} {}_{sr1}^{r1}\mathbf{R}^T \quad (3.4)$$

As the foot is assumed to be a rigid body segment, the foot and toe frames are aligned where the rotation matrix between these body frames forms an identity

matrix (${}_{r4}^3\mathbf{R} = \mathbf{I}$). The velocity and the height of the root joint are estimated by propagating from the toe frame (Section 3.2.3).

- 4) Formulate the homogenous transform between neighboring body frames (${}_{r1}^0\mathbf{T}, \dots, {}_{r4}^3\mathbf{T}$), i.e.

$${}_{r1}^0\mathbf{T} = \begin{bmatrix} {}_{r1}^0\mathbf{R} & {}^0\mathbf{P}_{r1} \\ \mathbf{0}_{1 \times 3} & 1 \end{bmatrix}. \quad (3.5)$$

- 5) Formulate the homogenous transform with respect to the pelvis body frame (${}_{r1}^0\mathbf{T}, \dots, {}_{r4}^0\mathbf{T}$).

- 6) Formulate ${}^N_0\mathbf{T}$ with the estimated root joint position ${}^N\mathbf{P}_0$ (Section 3.2.4) as follows:

$${}^N_0\mathbf{R} = {}^N_{s0}\mathbf{R} {}^0_{s0}\mathbf{R}^T \quad (3.6)$$

$${}^N_0\mathbf{T} = \begin{bmatrix} {}^N_0\mathbf{R} & {}^N\mathbf{P}_0 \\ \mathbf{0}_{1 \times 3} & 1 \end{bmatrix}. \quad (3.7)$$

- 7) Compute the homogenous transform with respect to the navigation frame (${}_{r1}^N\mathbf{T}, \dots, {}_{r4}^N\mathbf{T}$), i.e.

$${}_{r1}^N\mathbf{T} = {}^N_0\mathbf{T} {}_{r1}^0\mathbf{T}. \quad (3.8)$$

- 8) Obtain the positions of the body frames from ${}^N_0\mathbf{T}, \dots, {}_{r4}^N\mathbf{T}$.

3.2.3 Ground Contact Measurements

With the BM's parameters obtained using the estimated orientations from the IMUs (Section 3.2.1), the velocity and height of the root joint (i.e. waist) are estimated during the stance phase [24]. Herein, these measurements are denoted as the BM measurements. The proposed algorithm deploys the following angular rate energy detector to detect the stance phase with the foot-mounted IMU [36]:

$$D(\mathbf{z}_G(n)) = \frac{1}{N_G} \sum_{k=n-(N_G-1)/2}^{n+(N_G-1)/2} \|\mathbf{y}_G(k)\|^2 < \gamma_G \quad (3.9)$$

where $\mathbf{z}_G(n) = \{\mathbf{y}_G(k)\}_{k=n-(N_G-1)/2}^{n+(N_G-1)/2}$ is the measurement sequence, N_G is the window size, $\mathbf{y}_G(k)$ is the tri-axial gyroscope measurement, and γ_G is the detection threshold.

Zero height of human toe (i.e. contacting the ground) is represented by setting the third element of ${}^N\mathbf{P}$ to zero. During the stance, the height of the root joint is the third element of ${}^N\mathbf{P}_0$, which is calculated by

$${}^N\mathbf{P}_0 = {}^N\mathbf{T}{}^{r4}\mathbf{P}_0 \quad (3.10)$$

where ${}^N\mathbf{T}$ is formulated using ${}^{r4}\mathbf{R}$ and ${}^{r4}\mathbf{P}$.

The velocity of the toe body frame with respect to the pelvis body frame ${}^0\mathbf{v}_{r4}$ is then estimated as follows:

$${}^0\mathbf{v}_{r4} = {}^0\mathbf{v}_0 + \sum_{i=0}^3 {}^0\mathbf{R}({}^{ri}\boldsymbol{\omega}_{ri} \times {}^{ri}\mathbf{P}_{r(i+1)}) \quad (3.11)$$

where ${}^{ri}\boldsymbol{\omega}_{ri} (= {}^{ri}\mathbf{R}{}^{sri}\boldsymbol{\omega}_{sri})$ is the angular velocity of the body frame i . In (3.11), 0 and $s0$ are denoted as $r0$ and $sr0$. With the stationary foot velocity ${}^0\mathbf{v}_{r4} (= \mathbf{0}_{3 \times 1})$, the velocity of the root joint with respect to its body frame ${}^0\mathbf{v}_0$ is calculated as follows [37]:

$${}^0\mathbf{v}_0 = - \sum_{i=0}^3 {}^0\mathbf{R}({}^{ri}\boldsymbol{\omega}_{ri} \times {}^{ri}\mathbf{P}_{r(i+1)}). \quad (3.12)$$

Finally, the velocity of the root joint in the navigation frame ${}^N\mathbf{v}_0$ can be estimated by

$${}^N\mathbf{v}_0 = {}^N\mathbf{R}{}^0\mathbf{v}_0. \quad (3.13)$$

3.2.4 Robust Kalman Filter

In the proposed robust KF, the position of the root joint (waist) is estimated with the UWB, IMU, and BM measurements. The states are the 3D position and velocity of the root joint. As the states of each axis are independent of each other, the states \mathbf{x}_k ($= [x_k \ \dot{x}_k]^T$) are set for each axis, where x_k and \dot{x}_k are the position and velocity, respectively. This section only considers capturing the states in the X -axis, and the states of the other axes can similarly be estimated. The robust KF can be derived as the following linear discrete-time system:

$$\mathbf{x}_k = \mathbf{F}_{k-1}\mathbf{x}_{k-1} + \mathbf{G}_{k-1}u_{k-1} + \mathbf{v}_{k-1} \quad (3.14)$$

$$\mathbf{z}_k = \mathbf{H}_k\mathbf{x}_k + \mathbf{w}_k \quad (3.15)$$

where \mathbf{F}_{k-1} and \mathbf{G}_{k-1} are the state transition and input matrices; u_{k-1} is the input; \mathbf{v}_{k-1} and \mathbf{w}_k are the process and measurement noise vectors; \mathbf{z}_k is the measurement vector; and \mathbf{H}_k is the observation matrix. The model is set as the DWNA where the variables are defined as follows [26]:

$$\mathbf{F}_{k-1} = \begin{bmatrix} 1 & \Delta t \\ 0 & 1 \end{bmatrix} \quad (3.16)$$

$$\mathbf{G}_{k-1} = [\Delta t^2/2 \ \Delta t]^T \quad (3.17)$$

$$u_{k-1} = {}^N a_{k-1} \quad (3.18)$$

where Δt is the sampling period of the IMU, and ${}^N a_{k-1}$ is the first component of the external acceleration vector corresponding to X -axis, ${}^N \mathbf{a}_{k-1}$ ($= {}_{S0}^N \mathbf{R}_{k-1} {}^{S0} \mathbf{a}_{k-1} - {}^N \mathbf{g}$). ${}^N \mathbf{g}$ ($= [0 \ 0 \ g]^T$) is the gravity vector in the navigation frame where g is 9.81 m/s^2 . \mathbf{Q}_{k-1} is process noise covariance with following characteristics:

$$\mathbf{Q}_{k-1} = \begin{bmatrix} \Delta t^4/4 & \Delta t^3/2 \\ \Delta t^3/2 & \Delta t^2 \end{bmatrix} \sigma_v^2 \quad (3.19)$$

where σ_v^2 is the variance of the process noise.

Algorithm 3.1. Robust KF

```
1: for  $k = 1, \dots, n$ 
2:   Predict state
3:    $\hat{\mathbf{x}}_k^- = \mathbf{F}_{k-1}\hat{\mathbf{x}}_{k-1}^+ + \mathbf{G}_{k-1}u_{k-1}$ 
4:    $\mathbf{P}_k^- = \mathbf{F}_{k-1}\mathbf{P}_{k-1}^+\mathbf{F}_{k-1}^T + \mathbf{Q}_{k-1}$ 
5:   Initialize posteriori states and covariance
6:    $\hat{\mathbf{x}}_k^+(0) = \hat{\mathbf{x}}_k^-$ 
7:    $\mathbf{P}_k^+(0) = \mathbf{P}_k^-$ 
8:   for  $i = 1, \dots, m$ 
9:      $z_k^-(i) = \mathbf{H}_k(i)\hat{\mathbf{x}}_k^+(i-1)$ 
10:     $S_k(i) = \mathbf{H}_k(i)\mathbf{P}_k^+(i-1)(\mathbf{H}_k(i))^T + R_k(i)$ 
11:     $v_k(i) = z_k(i) - z_k^-(i)$ 
12:    NIS Test: Update innovation covariance
13:     $\gamma_k(i) = (v_k(i))^2/S_k(i)$ 
14:    if  $\gamma_k(i) > \chi_{\alpha,m}^2$ 
15:       $\lambda_k(i) = \frac{\gamma_k(i)}{\chi_{\alpha,m}^2}$ 
16:       $S_k(i) = \lambda_k(i)S_k(i)$ 
17:    end if
18:    Process  $i^{\text{th}}$  measurement
19:     $\mathbf{K}_k(i) = \mathbf{P}_k(i-1)\mathbf{H}_k(i)/S_k(i)$ 
20:     $\hat{\mathbf{x}}_k^+(i) = \hat{\mathbf{x}}_k^+(i-1) + \mathbf{K}_k(i)v_k(i)$ 
21:     $\mathbf{P}_k^+(i) = \mathbf{P}_k^+(i-1) - \mathbf{K}_k(i)\mathbf{H}_k(i)\mathbf{P}_k^+(i-1)$ 
22:  end for
23:  Assign posterior estimate and covariance
24:   $\hat{\mathbf{x}}_k^+ = \hat{\mathbf{x}}_k^+(m)$ 
25:   $\mathbf{P}_k^+ = \mathbf{P}_k^+(m)$ 
26: end for
```

The above robust KF is derived based on [38] and [39]. In this filter, the NIS test is used to detect the outlying measurements and softly reject them by inflating the

measurement noise covariance. Algorithm 3.1 shows an implementation of the proposed robust KF in pseudo-code.

The time-update equations in Lines 3 to 4 of Algorithm 3.1 are identical to the standard KF (Appendix A) [26], [27]. In Line 14, the NIS test is deployed as a one-sided hypothesis test to detect the outlier. If the equations (3.14) and (3.15) hold, the m -dimensional measurement \mathbf{z}_k should be normally distributed with its mean as the measurement prediction \mathbf{z}_k^- and variance as the innovation covariance \mathbf{S}_k : $\mathbf{z}_k \sim N(\mathbf{z}_k^-, \mathbf{S}_k)$ [38]. The NIS M_k^2 is the square of the Mahalanobis distance from observation \mathbf{z}_k to predicted state \mathbf{z}_k^- as following:

$$M_k^2 = (\mathbf{z}_k - \mathbf{z}_k^-)^T \mathbf{S}_k^{-1} (\mathbf{z}_k - \mathbf{z}_k^-). \quad (3.20)$$

Under (3.14) and (3.15), the NIS should be distributed in a chi-square with m degrees of freedom [38]. The hypothesis test is deployed to validate if the observed measurement is compatible with the model. The test statistics γ_k of the hypothesis test is set as the NIS. The null hypothesis H_0 states that the measurement noise covariance matches with the model, and the alternative hypothesis test H_a states that the measurement noise covariance is larger than expected. If the test statistics γ_k is larger than the quantile $\chi_{\alpha, m}^2$, set by the significance level α and m , H_0 is rejected. For example, when $\alpha = 0.05$ and $m = 1$, $\chi_{\alpha, m}^2$ is 3.84 [26]. Rejecting H_0 concludes that the outliers exist in the measurements. In this case, many of the recent works simply reject the measurements [40], [41]. As shown in Line 16, the proposed approach treats the outliers in a soft manner by inflating the innovation covariance $S_k(i)$ with a scaling factor $\lambda_k(i)$ [38]. These will also inflate the measurement noise covariance $R_k(i)$ (Line 10). Line 15 shows an analytic approach to calculate λ_k [38].

However, a single scaling factor $\lambda_k(i)$ can potentially be an issue if \mathbf{z}_k is multi-dimensional. If H_0 is rejected given the outlier in a single measurement, $\lambda_k(i)$ is adjusted for a whole measurement vector, and therefore all of \mathbf{z}_k is rejected. Instead of processing the measurements as a vector, the measurements are processed one at a time in the sequential KF structure from Lines 6 to 25 [27], [39].

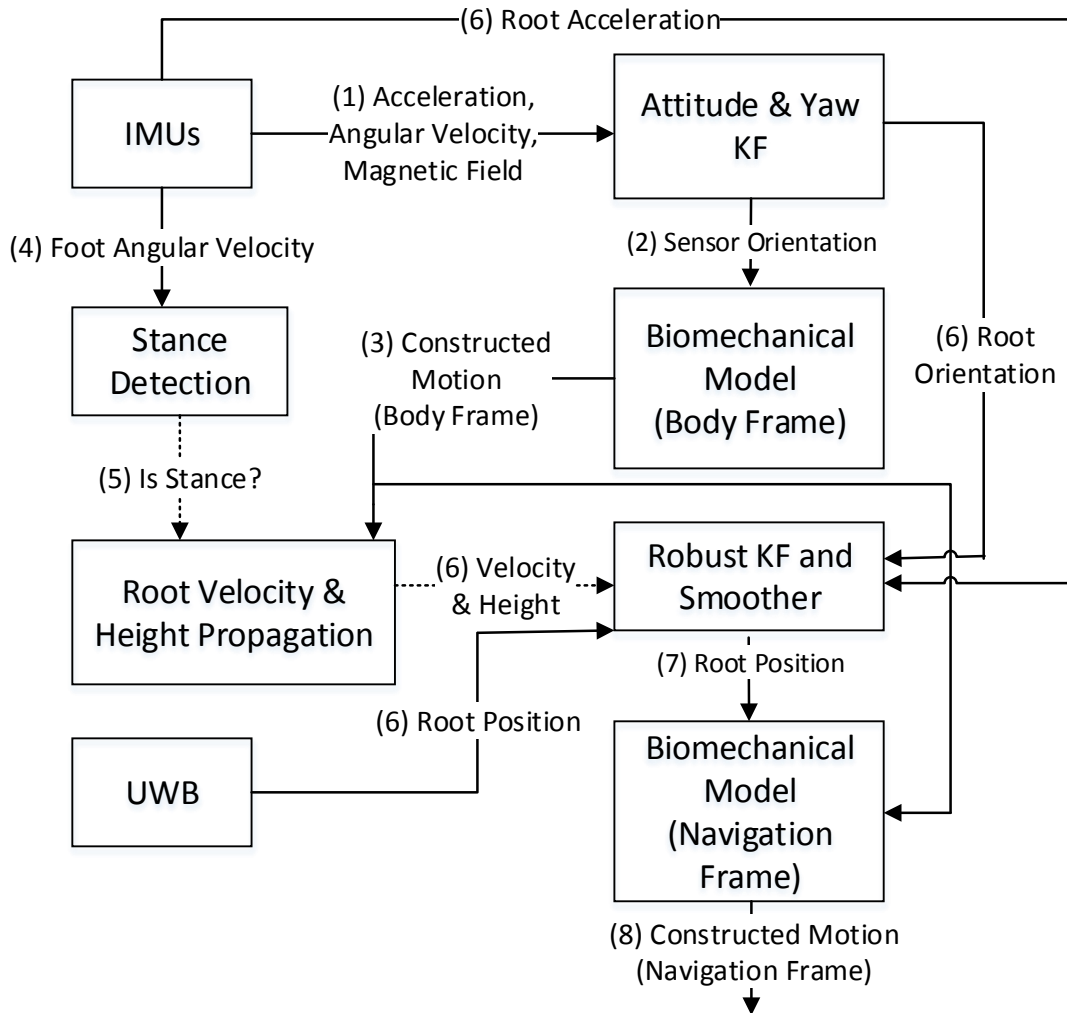


Figure 3.2. Overview of the proposed algorithm: (1)-(2) 3D orientations on the seven lower body segment are estimated with the attitude and yaw KF using the inertial and magnetic signals (Section 3.2.1); (3) the lower body motion with respect to the body frame is captured using the 3D orientations on the body segments (Section 3.2.2); (4)-(5) the stance phase is detected using the angular rate energy detector with the IMU at the foot (Section 3.2.3); (6)-(7) the position of the root joint is robustly estimated from the UWB position measurement, the external acceleration from the IMU, and the height and velocity measurements (during a stance phase) using the BM and can be post-processed with the RTS smoother (Section 3.2.4); and (8) the lower body motion with respect to the navigation frame is captured with the forward/smoothed root position (Section 3.2.2).

In the proposed robust KF, the UWB, velocity, and height measurements are processed in a sequence. The processing order did not matter as the states were estimated almost identically in any orders. The observation matrix \mathbf{H}_k is set to $[1 \ 0]$ for the UWB and height measurements and $[0 \ 1]$ for the velocity measurements. The measurement noise covariances $R_k(i)$ of the UWB, velocity, and height measurements are set as σ_{UWB}^2 , $\sigma_{velocity}^2$, and σ_{height}^2 , respectively. Both iterative and analytical approaches for calculating $\lambda_k(i)$ estimated the states almost identically, so the analytical method is chosen for the purposes of computational efficiency. In Table 1 [39], more reliable measurement with a smaller Mahalanobis distance is processed earlier to obtain better information about the states. However, the proposed robust KF skips this step as the filter estimate was almost identical with and without the step. We assume that these measurements are uncorrelated with each other, so the proposed robust KF does not use the Cholesky decomposition to decorrelate them [39]. For the post-processing, the RTS smoother (Appendix A) is deployed to improve the accuracy of the forward state estimate from the robust KF [27].

Compared to the conventional KF, the proposed algorithm adapts the sequential KF structure, so the matrix inversion is not required. This can save the computational time, making it suitable for the real-time application. The proposed robust KF is flexible – when more measurements are available on the root joint, they can be sequentially processed in a way similar to the proposed measurements.

The overview structure of the proposed algorithm is shown in Figure 3.2.

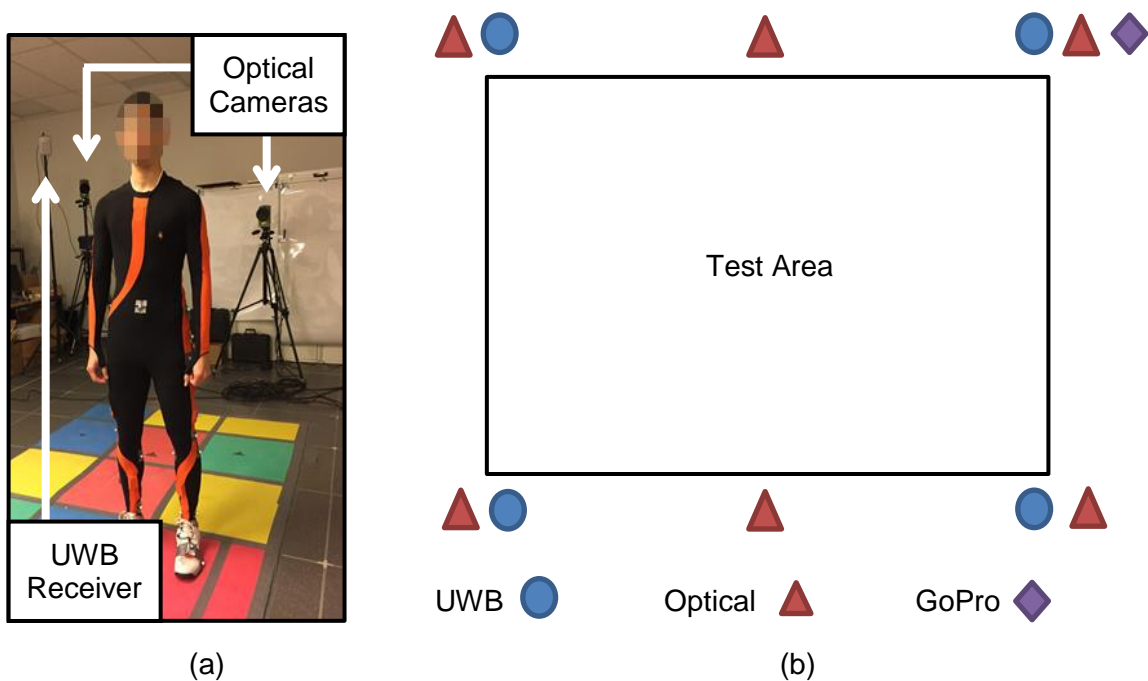


Figure 3.3. (a) Experimental setup with the test subject, UWB receiver, and optical cameras. The test subject is equipped with the MTx IMUs, the Ubisense UWB slim tag, and optical markers. (b) Test area with the UWB receivers, optical cameras, and the GoPro camera

3.3 Experimental Setup and Protocol

3.3.1 Experimental Setup

The performance of the proposed algorithm was tested in a 1.9×2.3 m rectangular-shaped test field in an indoor lab space (Figure 3.3). The subject wore seven MTx IMUs (from Xsens Technologies) including one IMU on the waist and six IMUs on the right and left thigh, shank, and foot; one UWB slim tag (from Ubisense) on the waist, and optical markers on the subject's body (including one on the waist) (Figure 3.1 and Figure 3.3(a)). Each MTx IMU includes a triaxial accelerometer, gyroscope, and magnetometer. The sampling rate was set at 100 Hz. All of the IMUs were connected to a Xbus Master where all of the signals were wirelessly transmitted to the computer. The UWB system consisted of four fixed anchor receivers (Series 7000 IP Sensors) and one mobile transmitter (Series 7000 Slim Tag). The UWB system estimates the 3D real-time

position of the slim tag by measuring both angle of arrival (AOA) and time difference of arrival (TDOA) from the tag's signal. The maximum allowable distance between the tag and receiver is 160 m, which is more than sufficient for the test area [42]. The sampling frequency of the UWB system was set at its highest value of 9.25 Hz. Four UWB receivers were placed on the corners of the test area (Figure 3.3(b)). An optical tracking system (from Qualisys), which has sub-millimeter accuracy, was used as the gold-standard reference system. A total of eight optical cameras were set around the test area (Figure 3.3(b)), and the sampling rate was set at 100 Hz. A GoPro Hero 3+ camera was employed to capture the subject's motion for a visual comparison, by placing it in the corner shown in Figure 3.3 (b).

3.3.2 Experimental Protocol

The subject was a 27 years old male with a height of 180 cm and a weight of 73 kg (Figure 3.3(a)). The dimensions of the lower body segments were measured as following: 35.3 and 12.5 cm for the waist width and height, 40.9 and 43.7 cm for the thigh and shank lengths, and 7.5 and 14.5 cm for the foot height and length (from the foot body frame to the ground-contacting toe body frame).

A total of 27 tests were conducted to study the performance of the proposed algorithm under various dynamic conditions. Each test lasted an average of 75 s. The tests included nine walking, three running, eight jumping, four kicking, and three stair climbing motions. Four of the nine walking tests involved two additional subjects randomly walking around the test area. These tests were conducted to simulate MoCap environments that are frequently crowded with other people. In these kinds of environments, the UWB signals can easily be attenuated and blocked by people in a crowd, so the positional accuracy suffers from a greater number of outliers and signal outages. Each half of the eight jumping tests involved the subject jumping and landing either with single or double legs. The kicking tests involved the subject randomly kicking with either right or left leg of his choice. In the stair testing, the subject walked up from the ground to the top of a 2-step stair and then jumped to the ground.

In the proposed algorithm, the following parameters need to be set: (i) σ_A^2 , σ_G^2 , σ_M^2 ,

c_A , and ε_M for the attitude and yaw KFs (Section 3.2.1), (ii) N_G and γ_G for the angular rate energy detector (Section 3.2.3), and (iii) α , m , σ_v^2 , σ_{UWB}^2 , σ_{height}^2 , and $\sigma_{velocity}^2$ for the robust KF (Section 3.2.4). σ_A^2 , σ_G^2 , and σ_M^2 were set as $10^{-4} \text{ m}^2/\text{s}^4$, $4 \times 10^{-5} \text{ rad}^2/\text{s}^2$, and 10^{-4} mT^2 , respectively. c_A was set to 0.1 which provides a good result for estimating the attitude under various dynamic conditions [28]. ε_M was set at 35 mT to distinguish the magnetic disturbance from the ferrous metal. N_G and γ_G were tuned to detect the stance phase by visually comparing against the GoPro camera and set to 15 and 2 rad/s, respectively. σ_v^2 was set at $10^2 \text{ m}^2/\text{s}^4$ based on a range of maximum acceleration magnitude a_M as $0.5a_M \leq \sigma_v \leq a_M$ [26]. α was set to 0.05 which has widely been used in the literature [43]. m was set as 1 as the measurements are singularly processed. σ_{UWB}^2 , σ_{height}^2 and $\sigma_{velocity}^2$ were set as 10^{-2} m^2 , 10^{-2} m^2 , and $1 \text{ m}^2/\text{s}^2$, respectively.

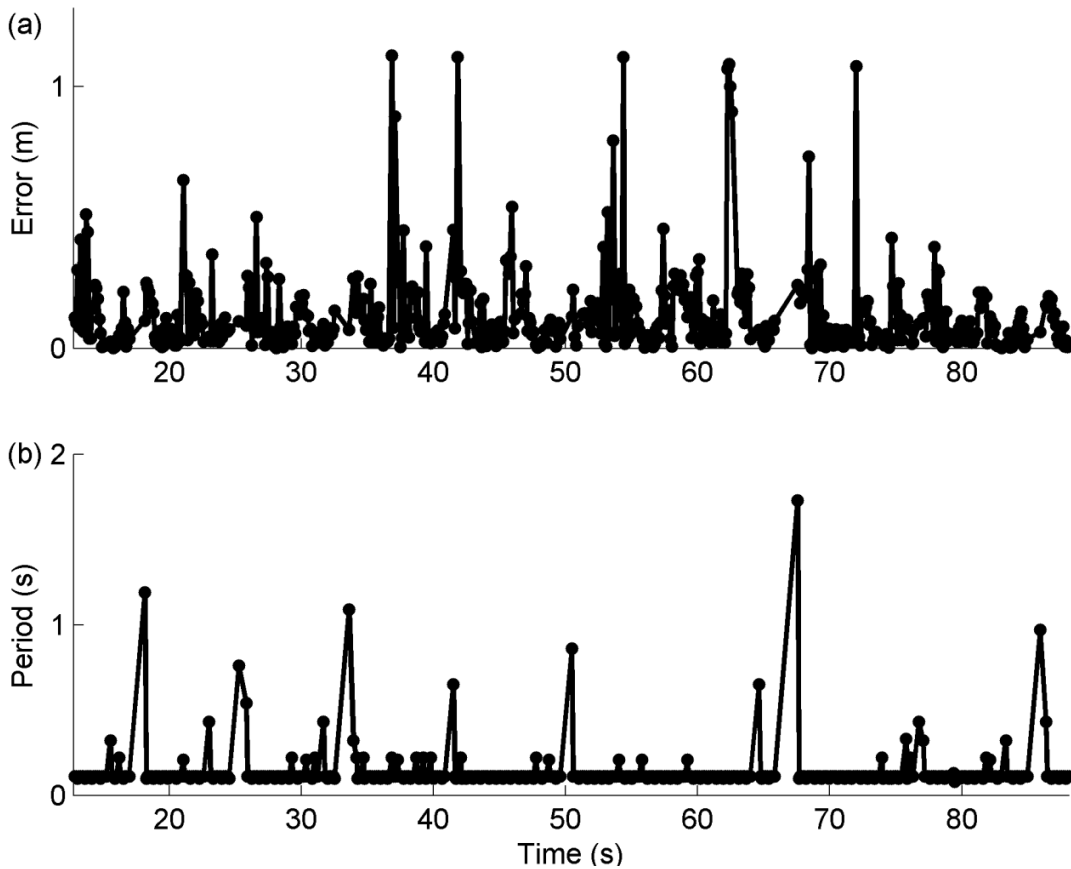


Figure 3.4. Results of the walking experiment: (a) UWB estimation error and (b) sampling period

The above experimental protocol was approved by the Office of Research Ethics of Simon Fraser University (Appendix D).

3.4 Experimental Results and Discussion

In this section, the commonly-encountered UWB errors are discussed first in Section 3.4.1. In Section 3.4.2, the two parameters conditions, such as the NIS test and BM velocity measurements, are examined. In Section 3.4.3, the performance of the proposed algorithm was compared to other outlier rejection algorithms based on the IAE and the reported DOP from the UWB system.

3.4.1 UWB Estimation Errors

Herein, the walking experiment where two subjects walking around the test area will be used as a primary test to verify the performance of the proposed algorithm. This environment/situation is frequently experienced in our daily lives, where the UWB system can frequently experience outliers and signal outages due to the NLOS and multipath. For example, in the 75.34 s walking experiment (Figure 3.4), the 6.32% of the UWB measurements were infected with the heavy-tailed outliers (errors > 30 cm), and the short signal outage (> 0.5 s) happened 9 times. These outliers violate the models (3.14) and (3.15) because only 0.27% of the measurements should be three standard deviations away from the zero-mean UWB noise distribution σ_{UWB} (=0.1 m) [43]. Given this non-Gaussian phenomenon, the conventional KF will not be robust against these outliers.

As shown in Figure 3.5(a)-(c), the UWB estimation errors are classified into three main categories: the outlier, sequential outliers, and signal outage. The outlier happens when the UWB measurement deviate significantly from the reference (i.e. absolute error of 1.12 m at 36.86 s). The sequential outliers are defined when the UWB experiences multiple outliers in a sequence (i.e. average error of 1.01 m from $t= 62.26$ s to 62.58 s). The UWB experiences a signal outage when the UWB measurements are not available for a short period of time (i.e. $t= 65.84$ s to 67.55 s).

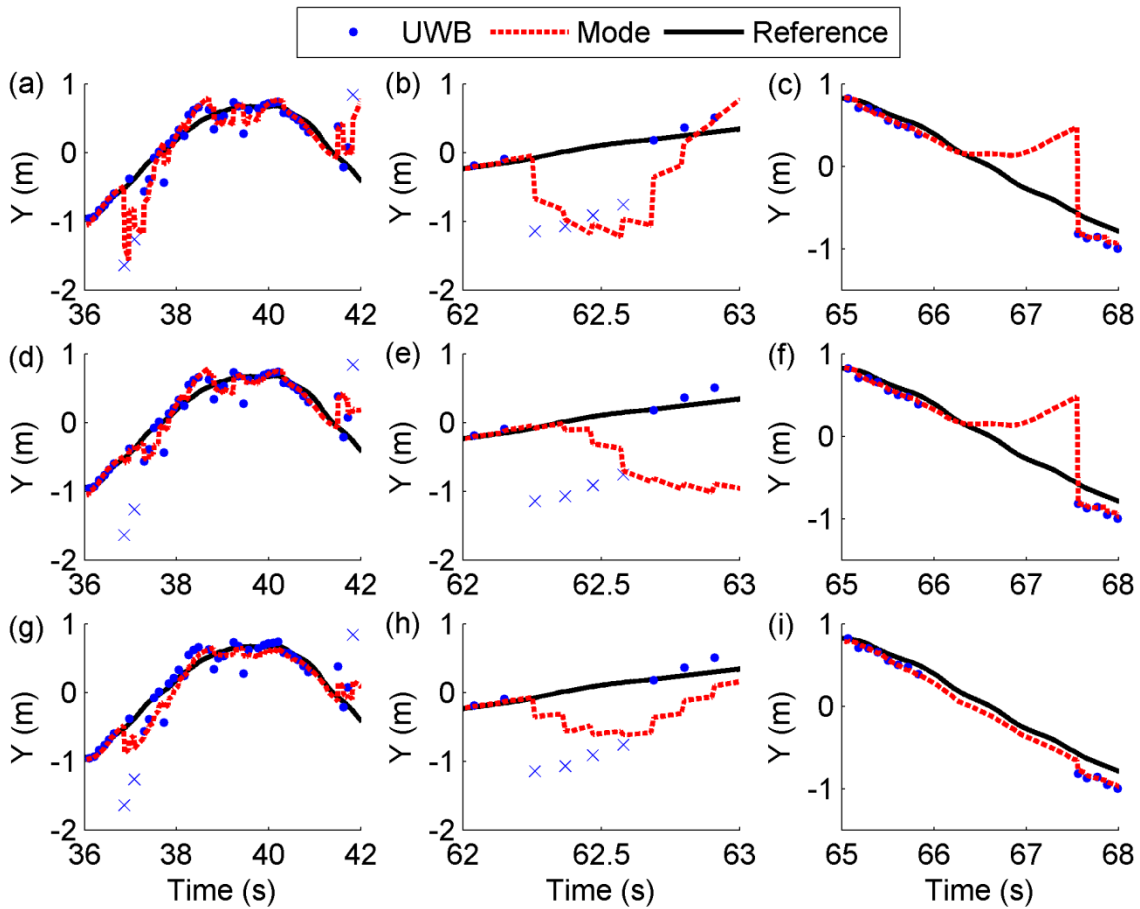


Figure 3.5. Position estimates from the UWB, Mode 1 (a)-(c), Mode 2 (d)-(f), and Mode 3 (g)-(i), and the reference camera system. The columns are based on the types of the UWB measurement errors. The first, second, and third columns are the UWB's outliers ($t= 36.86, 37.08,$ and 41.83 s), four sequential outliers ($t= 62.26$ to 62.58 s), and the 1.71 s signal outage ($t= 65.84$ to 67.55 s), respectively. The UWB outliers are shown by the blue \times symbols. Table 3.1 summarizes the criterion for the above three modes.

3.4.2 Parameters

In this section, the effect of the NIS test and the BM measurements are investigated with three different modes. Mode 1 estimates the position with the IMU and UWB measurements and assumes the constant UWB measurement noise covariances. Mode 1 is deployed as a benchmark to compare against for Modes 2 and 3. Modes 2 and 3 are similar to Mode 1, but Mode 2 adapts the UWB measurement noise covariances with the NIS test. Mode 3 additionally calculates the position with the BM

measurements. Table 3.1 summarizes the measurements and criteria for these modes.

In Mode 1, the position was not accurately estimated against the reference trajectory in all of the UWB error categories. The estimated trajectory resulted in large errors during both the outliers and sequential outliers (Figure 3.5(a)-(b)). With the constant measurement noise covariance, the measurements were equally weighted in the presence of the outliers. During the signal outage, the estimated position exponentially diverged over time from the reference trajectory with a maximum error of 1.05 m at $t = 67.55$ s (Figure 3.5(c)). This is due to the double-integration of the external acceleration from the IMU measurement [44]. A small error and bias in the acceleration measurement could potentially yield a large position drift in the output.

In Mode 2, the position was robustly estimated in the presence of the outliers (Figure 3.5(d)). The UWB measurement noise covariance was inflated to reduce its weight when the outliers were present (Figure 3.6(a)). However, it was not robust against the sequential outliers, and the position state diverged from the reference trajectory after the outliers (Figure 3.5(e)). First three sequential outliers were correctly detected, and the measurement noise covariances were inflated accordingly (Figure 3.6(b)). However, during the sequential outliers, Mode 2 relied on the IMU measurement, where the state diverged over time. After the sequential outliers, the UWB measurements were rejected due to a large NIS between the position state and the measurement. During the signal outage, like Mode 1, the position state exponentially diverged over time due to the estimation with the IMU (Figure 3.5(f)).

Table 3.1. Six Estimation Modes of the Robust KF

Modes	Measurements			Criteria		
	UWB	IMU	BM	Innovation	DOP	NIS
1	✓	✓				
2	✓	✓				✓
3	✓	✓	✓			
4	✓	✓	✓	✓		
5	✓	✓	✓		✓	
6	✓	✓	✓			✓

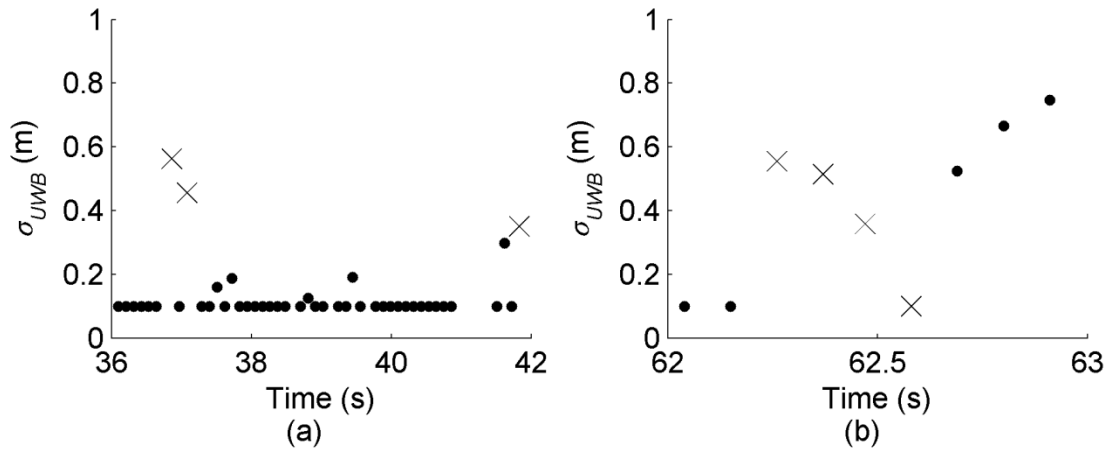


Figure 3.6. Standard deviation of the UWB measurement noise covariance during (a) the outliers ($t= 36.86, 37.08, \text{ and } 41.83 \text{ s}$) and (b) four sequential outliers ($t= 62.26 \text{ to } 62.58 \text{ s}$) with Mode 2. The outliers are shown by black \times symbols.

In Mode 3, the position estimation was not robust against the outliers and the sequential outliers due to the constant weight of the UWB measurements (Figure 3.5(g)-(h)). During the signal outage, the position error grew slower compared to the Modes 1 and 2 (see Figure 3.5(i) in comparison to Figure 3.5(c) and (f)). The reason behind this is that the position could be estimated with single integrations of the BM velocity measurements, which were available 84% of the time during the 1.71 s outage period.

Based on the above results, we can conclude that the outliers can be correctly detected and weighted down with the NIS test. During the signal outage, the position was captured more accurately with the BM velocity against to the IMU measurements. The proposed algorithm is able to fuse these modalities to robustly estimate the position despite of the UWB outliers and signal outages.

3.4.3 Robust Filters

In this section, three outlier rejection approaches are explored: the IAE, the Ubisense dilution of precision (DOP), and the NIS test. All three methods deploy the IMU, UWB, and BM measurements, but the measurement noise covariance is estimated differently. In Mode 4, the covariances are estimated as the window-based innovation

sequence where the window size is set to 10, trading off between the biasness and the tractability of the estimate [31]. In Mode 5, the UWB measurement noise covariance is set according to the UWB DOP [6]. The Ubisense UWB system outputs a DOP for every estimated position. The DOP value indicates how well both the TDOA and the AOA measurements converge to each other. When the UWB position error was high, the DOP was generally high. The DOP scale was in the UWB positioning error, so σ_{UWB} is set to the DOP. The proposed algorithm is the Mode 6, where both UWB and BM measurement noise covariances are varied based on the NIS test. Table 3.1 summarizes the criterion for the above three modes.

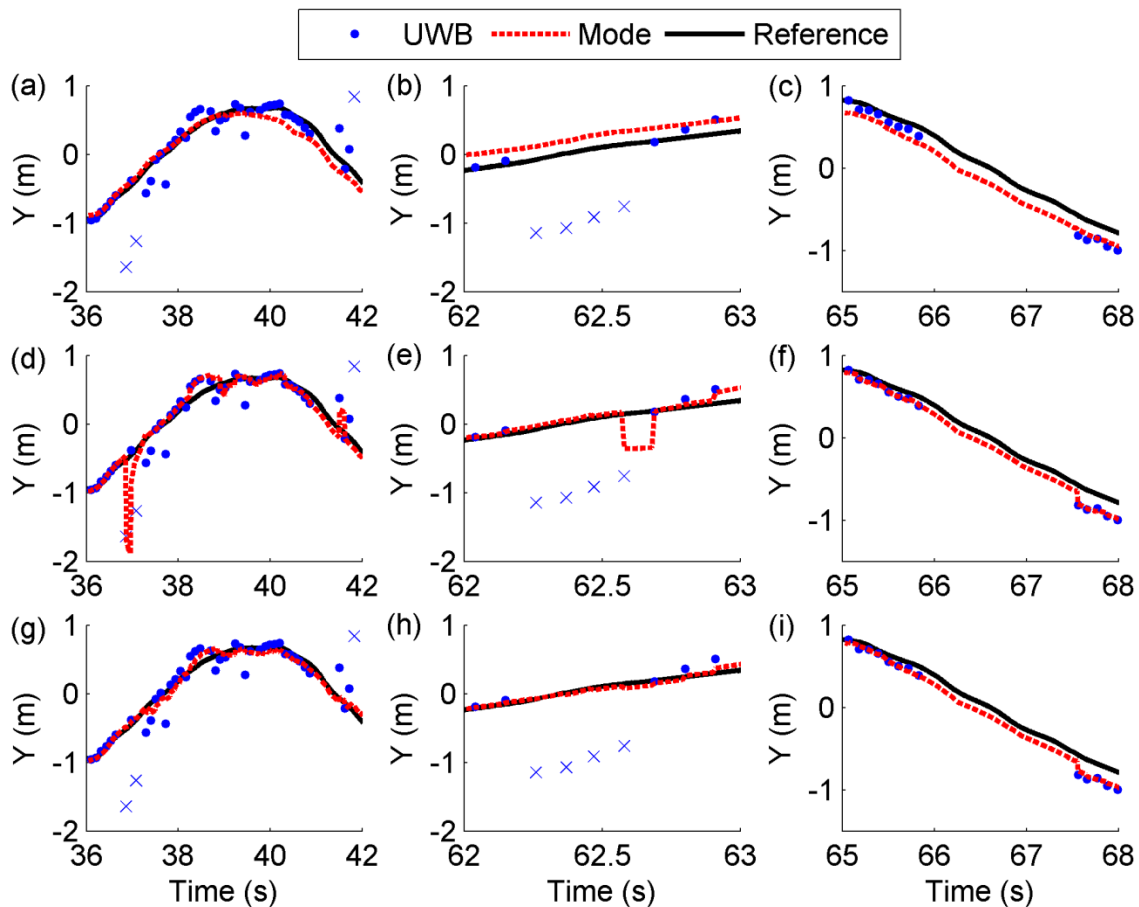


Figure 3.7. Position estimates from the UWB, Mode 4 (a)-(c), Mode 5 (d)-(f), and Mode 6 (g)-(i), and the reference on the Y -axis. The columns are based on the types of the UWB measurement errors and are explained in the Figure 3.5 description. The UWB outliers are shown by blue \times symbols.

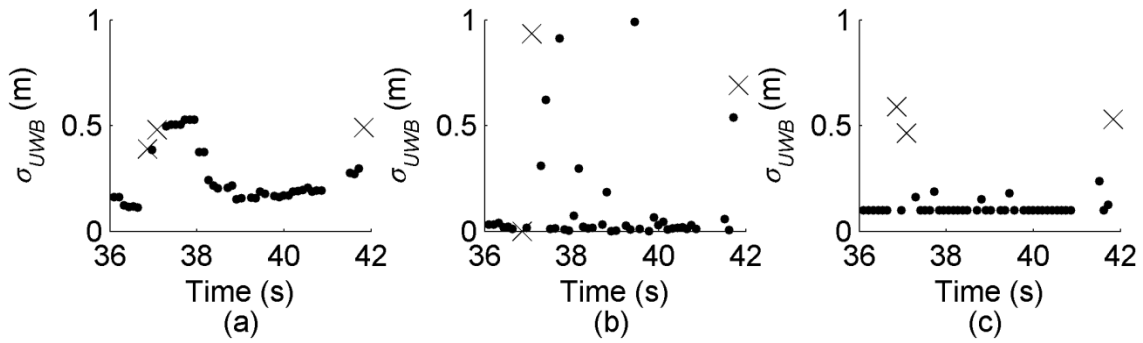


Figure 3.8. Standard deviation of the UWB measurement noise covariance with Modes 4 (a), Mode 5 (b), and Mode 6 (c) during the outliers ($t= 36.86$, 37.08 , and 41.83 s). The outliers are shown by black \times symbols.

Mode 4 was able to detect the outliers and inflated the UWB measurement noise covariance accordingly (Figure 3.7(a)-(b)). However, due to its window-based method, both the past and current innovations impacted the current measurement noise covariance. For example, the UWB outlier at $t= 36.86$ s resulted in a large innovation. Given the window size of 10, this innovation impacted the next 9 subsequent data (until $t= 37.94$ s), where all of σ_{UBW} were set greater than 0.35 m (Figure 3.8(a)). Furthermore, the covariances were not accurately captured even after some period of the outliers. For example, the UWB system did not output an outlier from $t= 39.56$ to 40.86 s, but all of σ_{UBW} were bigger than the expected σ_{UBW} ($=0.1$ m) with an average of 0.18 m. As a result, these measurements were rejected with smaller weights, and the IMU and BM velocity measurements were relied more, so the position state slowly diverged. As shown in Figure 3.7(c), the position was robustly tracked during the signal outage, but the error remained constant from the start of the outage.

Mode 5 was not robust against some outliers (Figure 3.7(d)-(e)). At $t= 36.86$ s, the DOP of the UWB outlier was set to 0.00056 m (Figure 3.8(b)). This outlier, therefore, had a high weight, resulting in a large error of 1.12 m. The UWB measurement ($t= 38.16$ s) was not an outlier with a small absolute error of 4.1 cm, but this measurement was rejected due to a large DOP ($=0.30$). In the sequential outliers, this mode was robust for first three outliers, but not the last outlier at $t= 62.58$ s. The DOP value was set at 0.062 for the last outlier, so this UWB outlier had a high weight. Mode 5 was robust against the

signal outage, as the position was estimated with the BM velocity measurement (Figure 3.7(f)).

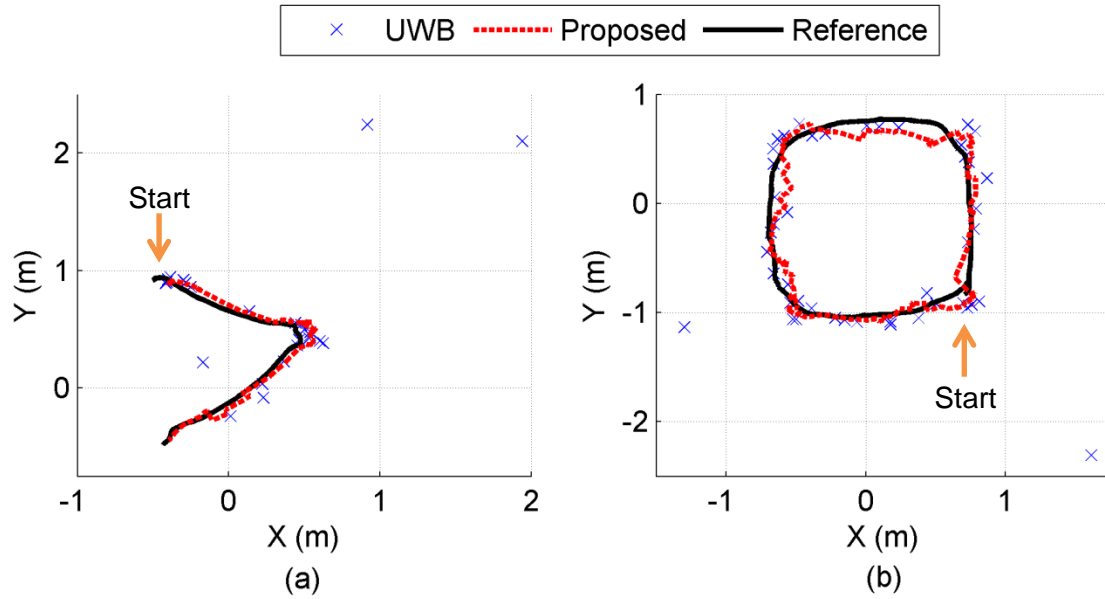


Figure 3.9. Horizontal trajectories of dynamic motions: (a) single-leg jumping and (b) running motions

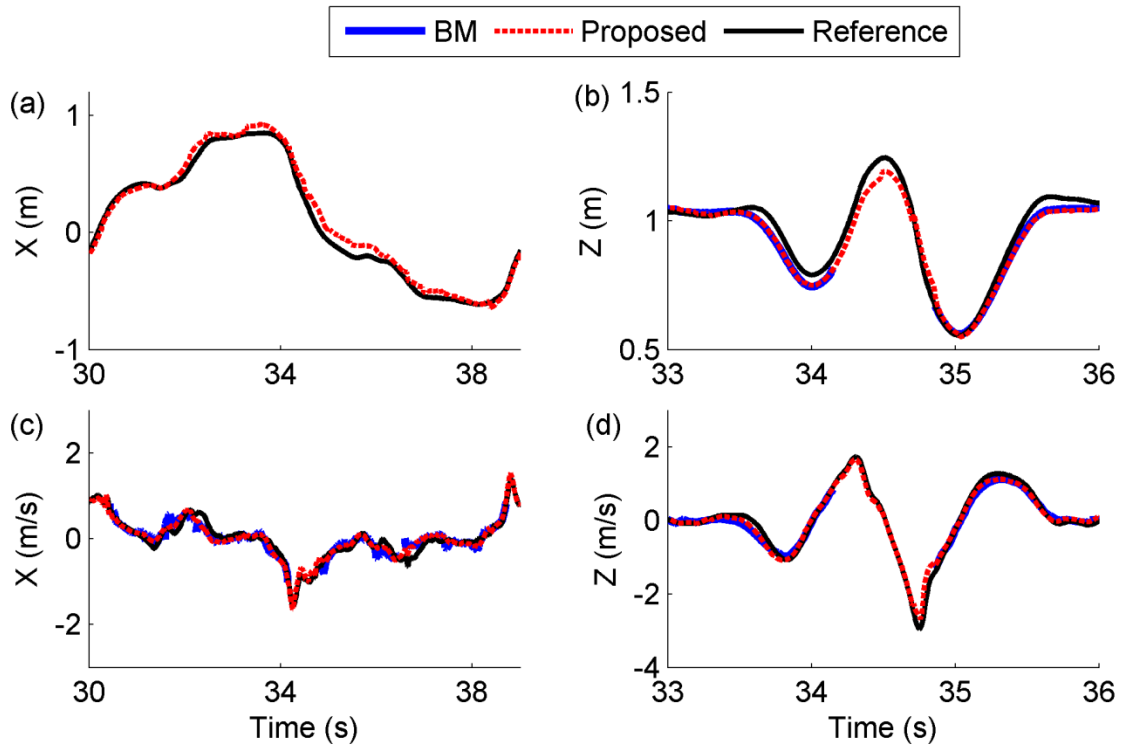


Figure 3.10. Position and velocity estimates on (a), (c) X-axis and (b), (d) Z-axis for double-leg jumping

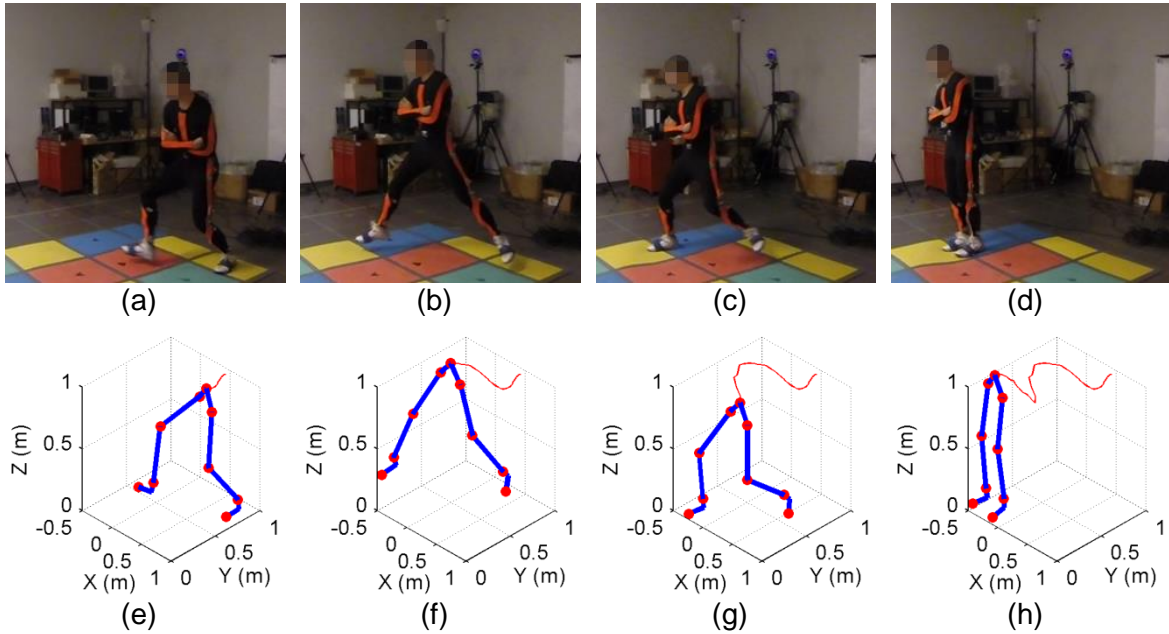


Figure 3.11. Single-leg horizontal jump motion (a)-(d) captured by the GoPro camera and (e)-(h) constructed using the proposed algorithm. The jump cycle is broken into four phases: (a), (e) the start of the jump, (b), (f) the lift-off, and (c), (g) the ground-contact, and (d), (h) the end of jump.

In Mode 6, the position was robustly estimated for all of the UWB error categories (Figure 3.7(g)-(i)). High σ_{UWB} (>0.45 m) was assigned to the UWB outliers at $t= 36.86$, 37.08 , and 41.83 s (Figure 3.8(c)). As a result, the proposed algorithm was able to detect these measurements as the outliers and softly rejected them. Similarly, the proposed algorithm correctly rejected the sequential outliers with high σ_{UWB} and closely followed the reference trajectory. It was also robust against the signal outage, as the position was estimated with single integrations of the BM velocity measurements. Similar to the Y-axis, the UWB measurements were infected with frequent large noise in the 2D horizontal trajectories (Figure 3.9). The proposed algorithm robustly estimated the position during the dynamic motion, such as single-leg zigzag jumping and running. During the dynamic motion (double-leg jumping), the proposed algorithm robustly estimated both position and velocity in the horizontal and vertical trajectories (Figure 3.10). Compared to the UWB measurements, most of the BM measurements closely followed the reference trajectory and were not prone to the outliers. Based on the results from all of the experiments, almost all of the height and velocity measurements

(>99.99%) were not classified as outliers with the NIS test. The reason is that the measurements were obtained from the IMUs whose noises are normally distributed [28]. The BM measurement noise covariances can be potentially set to constant values for the computational purpose if desired.

The proposed algorithm accurately captured the lower-body motion against the one visually from the GoPro camera during the dynamic motion, such as a single-leg horizontal jumping (Figure 3.11). Given the high reported accuracy of the attitude and yaw KFs [5], [7], [28], the accuracy for the joint angles was reported to be less than 3.5° for the walking and jumping experiments [6].

Table 3.2 presents the RMSE of the UWB and BM measurements for all of 27 conducted tests. The UWB 3D position accuracy was 29.6 cm, which was mainly inflated due the frequent outliers. The BM measurements accurately tracked the reference trajectory with centimeters-level accuracy and were not prone to the outliers.

Table 3.2. RMSE of the UWB and BM Measurements

UWB				BM				
Position (cm)				Velocity (cm/s)			Height (cm)	
X	Y	Z	3D	X	Y	Z	3D	Z
18.4	19.0	12.9	29.6	17.7	16.8	9.2	26.3	3.3

Table 3.3. RMSE of the Position Tracking With Six Estimation Modes of the Robust KF

Modes	Forward (cm)				Smoothing (cm)			
	X	Y	Z	3D	X	Y	Z	3D
1	19.6	21.4	13.5	32.3	11.3	11.9	7.5	18.2
2	12.3	13.1	8.6	20.2	8.1	8.9	5.5	13.5
3	12.2	12.9	4.4	18.5	9.5	9.7	3.4	14.2
4	11.4	11.7	3.5	16.9	9.6	10.4	3.3	14.8
5	9.9	10.1	5.6	15.4	8.2	8.9	4.6	13.1
6	8.1	8.8	3.7	12.7	7.1	7.7	3.2	11.1

Table 3.4. RMSE of the Position Tracking for Two Activity Types Using Mode 6

Tests	UWB (cm)				Forward (cm)			
	X	Y	Z	3D	X	Y	Z	3D
Walking	17.2	17.5	9.7	26.5	6.3	6.2	2.6	9.2
Dynamic	19.2	19.3	14.6	31.0	8.6	8.6	4.0	12.9

Table 3.3 shows the RMSE of the forward and smoothing estimates of six discussed modes for all of 27 conducted tests. The performance of the proposed algorithm (Mode 6) clearly dominates the other modes for both forward and smoothing estimation. Compared to the raw UWB data, the horizontal and vertical position accuracy is improved by 54.7% and 71.5% for the forward estimate and 60.6% and 75.0% for the smoothing estimate, respectively. With the smoother, the 3D position accuracy is further improved by 12.2%.

Table 3.4 compares the positioning accuracies of the UWB and forward estimates of the proposed algorithm (Mode 6) of the physical activities with two different intensity levels. For these activities, the environment was kept the same with the test subject alone. All of the running, kicking, and jumping tests are categorized as dynamic activities. Compared to the UWB system, the positioning accuracies improved with the proposed algorithm (by over 55% in all directions). The accuracy of the UWB system is also significantly degraded from slow to dynamic activities, especially in the vertical trajectory (23.4% greater than horizontal), but the proposed algorithm maintains similar accuracies (less than 2.5 cm and 36% in all directions). Compared to the UWB data, the 3D positioning accuracy improved by 65.3% and 58.4% for the slow and fast motion activities, respectively.

3.5 Conclusion

This chapter introduced a robust method to accurately track the lower body motion by fusing the wearable sensor measurements including inertial/magnetic sensors and UWB positioning system. The UWB positioning system frequently experiences outliers and signal outages due to multipath and the NLOS condition. The proposed algorithm addressed the outliers by detecting and weighting them using the NIS test and

processing the available accurate measurements at the root joint (waist) sequentially. The algorithm does not require a manual turning and automatically scales the measurement noise covariance upon the outliers for individual measurements. Additionally, during the signal outage periods, the position can be estimated more accurately with the BM measurements compared to the IMU measurements. For this purpose, a homogenous transformation scheme is developed to systematically capture the lower body motion using the wearable IMUs. During the stance phase, the height/velocity of the stationary foot was propagated through the BM to estimate the height/velocity of the root joint. The experimental results show that the NIS test can correctly detect outliers and reduce its weights. In terms of the positioning accuracy, the proposed algorithm outperformed the outlier rejection based on the IAE and reported DOP from the UWB system.

Chapter 4.

Conclusion

4.1. Thesis Summary and Contributions

This thesis presented robust human motion tracking algorithms using the IMU and the wireless sensors, such as BLE and UWB. In Chapter 2, a novel indoor localization method using the BLE and IMU was developed. The trilateration residue was deployed to adaptively weight the estimates from these sensor modalities. Chapter 3 presented a robust sensor fusion algorithm for capturing lower body motion using UWB positioning system and wearable IMUs aided by a biomechanical model. The experimental results showed that the proposed algorithm can provide high accuracy for tracking the location of a human subject under various dynamic activities. The achievements and contributions of each chapter are summarized as follows.

Summary of Chapter 2

This chapter proposed a novel indoor localization method using the BLE and IMU. The multipath and NLOS errors from low-power wireless localization systems commonly result in outliers, affecting the positioning accuracy. This problem was addressed by adaptively weighting the estimates from the IMU and BLE in the proposed cascaded KF. The positioning accuracy was further improved with the RTS smoother. The performance of the proposed algorithm was compared against that of the standard KF experimentally. The results showed that the proposed algorithm can maintain high accuracy for position tracking the sensor in the presence of the outliers.

Summary of Chapter 3

This chapter proposed a robust sensor fusion algorithm to accurately track the location and capture the lower body motion under various dynamic activities, such as walking, running, and jumping. The position accuracy of the wireless positioning systems frequently suffers from NLOS and multipath effects, resulting in heavy-tailed outliers and signal outages. This problem is addressed by integrating the estimates from an UWB system and IMUs, but also taking advantage of the estimated velocity and height obtained from an aiding lower body biomechanical model. The outliers were detected for individual measurements using the NIS where the measurement noise covariance is softly scaled to reduce its weight. The positioning accuracy was further improved with the RTS smoother. The proposed algorithm was validated based on an optical motion tracking system for both slow (walking) and dynamic (running and jumping) activities performed in laboratory experiments. The results showed that the proposed algorithm can maintain high accuracy for tracking the location of a subject in the presence of the outliers and UWB signal outages with a combined 3D positioning error of less than 13 cm.

4.2. Future Recommendations

During this research, further works were identified and recommended as future works as follows.

BLE-based Localization

Compared to the high-motion activity protocol with the UWB system, the BLE system was tested in a small indoor space (70 cm by 80 cm) with a slow movement. However, it had an average horizontal RMSE of 43.3 cm which is 56.8% greater than that of UWB (Table 3.2). This shows that the narrowband technology (BLE) is more prone to the multipath and NLOS effects compared to the UWB system, which deploys a very short pulse to distinguish from reflected signal.

The BLE is popularly deployed in a growing number of smartphones for various applications, such as music streaming and wireless headsets. The BLE in smartphones makes the indoor positioning more practical. However, since the BLE antennas are inside smartphones, it will be likely to experience more NLOS, so the positioning accuracy will be much less accurate (a meter-accuracy) in comparison to the current proposed BLE/IMU prototype. Therefore, a future recommendation with these systems is to reliably locate the user with a room/meter-level accuracy using the threshold-based algorithm based the magnitudes of the RSSI measurements. The fingerprinting method is popularly used for this type of positioning where the position is estimated based on the statistical approach using prior collected RSSI measurements in known positions [19].

UWB/IMU-based Motion Capture

The proposed UWB/IMU MoCap was able to accurately track the location and capture the lower body motion under various dynamic activities. Current proposed system included one UWB system at the waist, and the other body segments were constructed based on an inertial-based biomechanical construction. The body segment lengths may vary due to muscle movements, especially in high-speed activities. One recommendation is to place UWB tags on the other body segments, such as hip, knee, and ankle. These joint positions can be estimated by integrating the estimates from these UWB tags and an aiding biomechanical construction. Also, in the current experimental protocol, the sensor modules (IMU) were attached side by side to the body segments with the Velcro tapes. The modules attached over human skin may move during such rapid body movements. As a result, the relative position and orientation between the sensor frame and its corresponding body frame may slightly change during test motions. To ensure better attachment, the modules should be additionally strapped with the Velcro tapes around the body segments. The modules should also be placed near to the joints of the body segments with minimal muscle movements. Next, the proposed algorithm was verified against only one subject. The future work is to validate the proposed algorithm with more test subjects whose sizes are varied in a wider range. Moreover, given a large coverage of the UWB positioning system (i.e. about 20m by 20m), the proposed algorithm should be extended for real-life dynamic entertainment applications, such as gaming and filmmaking.

4.3. Benefits and Significance

MoCap has served as an essential technology to many industries, including entertainment (gaming and filmmaking), movement science (human factors and kinetics), virtual reality (training and simulations), and health (diagnostics and rehabilitation). In gaming and filmmaking, for example, the proposed MoCap can be used to record actions of human actors or athletes, and using that information to animate digital characters models in 3D computer animation. However, if MoCap devices can be miniaturized and truly become wearable and ambulatory, it can liberate a wealth of information that could have a substantial impact on our everyday lives. Our bodies, as well as our behaviors can generate a wealth of data for wearable sensors such as MEMS-based IMUs to collect and analyze, for example, during daily activities or sports. As wearable technology become more prominent, wireless connectivity technology that enable these devices to connect to smartphone are key to unlocking their true potential, which will foster new technological innovation across various industries in Canada.

References

- [1] Rohan, "3D Motion Capture System Market Worth 142.5 Million USD by 2020," Internet: www.marketsandmarkets.com/PressReleases/3d-motion-capture-system.asp [Nov. 2, 2015].
- [2] S. Twist. "Real-Time Facial Motion Capture System." Master's thesis, NCCA Bournemouth University, United Kingdom, 2010.
- [3] P.-Z. Chen, J. Li, M. Luo, and N.-H. Zhu, "Real-Time- Human Motion Capture Driven by a Wireless Sensor Network," *Int. Jour. Compt. Games. Tech.*, vol. 2015, pp. 1-14, Jan. 2015.
- [4] M. Ermes, J. Parkka, Jn. Mantyjav, and I. Korhonen, "Detection of daily activities and sports with wearable sensors in controlled and uncontrolled conditions," *IEEE Trans. Inf. Tech. Biomed.*, vol. 12, no. 1, pp. 20-26, Jan. 2008.
- [5] S. Zihajehzadeh, D. Loh, M. Lee, R. Hoskinson, and E. J. Park, "A cascaded two-step Kalman filter for estimation of human body segment orientation using MEMS-IMU", in *Proc. Ann. Int. Conf. IEEE Eng. Med. Bio. Soc. (EMBC)*, Chicago, USA, Aug. 2014, pp. 6270-6273.
- [6] S. Zihajehzadeh, P. K. Yoon, B.-S. Kang, and E. J. Park, "UWB-aided inertial motion capture for lower body 3-D dynamic activity and trajectory tracking," *IEEE Trans. Instrum. Meas.*, vol. 64, no. 12, pp. 3577-3587, Dec. 2015.
- [7] S. Zihajehzadeh, D. Loh, T. J. Lee, R. Hoskinson, and E. J. Park, "A cascaded Kalman filter-based GPS/MEMS-IMU integration for sports application," *Meas.*, vol. 73, pp. 200-210, May 2015.
- [8] T. Lupton and S. Sukkarieh, "Visual-inertial-aided navigation for high-dynamic motion in built environments without initial conditions," *IEEE Trans. Rob.*, vol. 28, no. 1, pp. 61-76, Feb. 2012.
- [9] M. El-Gohary and J. McNamara, "Shoulder and elbow joint angle tracking with inertial sensors," *IEEE Trans. Biomed. Eng.*, vol. 59, no. 9, pp. 2635-2641, Sept. 2012.
- [10] C. M. N. Brigante, N. Abbate, A. Basile, A. C. Faulisi, and S. Sessa, "Towards miniaturization of a MEMS-based wearable motion capture system," *IEEE Trans. Ind. Elect.*, vol. 58, no. 8, pp. 3234-3241, Aug. 2011.

- [11] S.-K. Kim, S. Hong, and D. Kim, "A walking motion imitation framework of a humanoid robot by human walking recognition from IMU motion data," in *Proc. IEEE-RAS Int. Conf. Hum. Rob.*, Paris, France, Dec. 2009, pp. 343-348.
- [12] A. G. Kirk, J. F. O'Brien, and D. A. Forsyth, "Skeletal parameter estimation from optical motion capture data," in *Proc. IEEE Conf. Comp. Vis. Pat. Recog.*, San Diego, USA, June 2005, pp. 782-788.
- [13] D. Lee and Y. Nakamura, "Mimesis scheme using a monocular vision system on a humanoid robot," in *Proc. IEEE. Int. Conf. Rob. Aut.*, Roma, Italy, Apr. 2007, pp. 2162-2168.
- [14] D. Roetenberg, P. J. Slycke, and P. H. Veltink, "Ambulatory position and orientation tracking fusing magnetic and inertial sensing," *IEEE Trans. Biomed. Eng.*, vol. 54, no. 5, pp. 883-890, May 2007.
- [15] X. L. Meng, Z.-Q. Zhang, J.-K. Wu, and W.-C. Wong, "Hierarchical information fusion for global displacement estimation in microsensor motion capture," *IEEE Trans. Biomed. Eng.*, vol. 60, no. 7, pp. 2052-2063, July 2013.
- [16] H. Fourati, "Heterogeneous data fusion algorithm for pedestrian navigation via foot-mounted inertial measurement unit and complementary filter," *IEEE Trans. Instrum. Meas.*, vol. 64, no. 1, pp. 221-229, Jan. 2015.
- [17] Q. Yuan and I. M. Chen, "3-D localization of human based on an inertial capture system," *IEEE Trans. Rob.*, vol. 29, no. 3, pp. 806-812, June 2013.
- [18] A. S. Paul and E. A. Wan, "RSSI-based indoor localization and tracking using sigma-point Kalman smoothers," *IEEE Trans. Sel. Top. Sig. Proc.*, vol. 3, no. 5, pp. 860-873, Oct. 2009.
- [19] D. Dardari, P. Closas, and D. M. Djuric, "Indoor tracking: theory, methods, and technologies," *IEEE Trans. Veh. Tech.*, vol. 64, no. 4, pp. 1263-1278, Apr. 2015.
- [20] K. Langendoen and N. Reijers, "Distributed localization in wireless sensor networks: a quantitative comparison", *Elsevier Computer Networks*, vol. 43, pp. 499-518, 2003.
- [21] G. Blumrosen, B. Hod, T. Anker, D. Dolev, and B. Rubinsky, "Enhancing RSSI-based tracking accuracy in wireless sensor networks", *ACM Trans. Sensor Networks*, vol. 9, no. 3, pp. 29:1-29:28, May 2013.
- [22] T. K. K. Tsang and M. N. El-Gamal, "Ultra-wideband (UWB) communications systems: an overview," in *Proc. IEEE Int. New Circ. Syst. Conf.*, Quebec City, Canada, June 2005, pp. 381-386.

- [23] L. Mucchi, F. Trippi, and A. Carpini, "Ultra wide band real-time location system for cinematic survey in sports," in *Proc. Int. Symp. App. Sci. Biomed. Comm. Tech.*, Rome, Italy, Nov. 2010, pp.1-6.
- [24] X. L. Meng, Z. Q. Zhang, S. Y. Sun, J. K. Wu, and W. C. Wong, "Biomechanical model-based displacement estimation in micro-sensor motion capture," *Meas. Sci. Tech.*, vol. 23, pp. 1-11, Mar. 2012.
- [25] S.P. Kwakkel, G. Lachapelle, and M.E. Cannon, "GNSS aided in situ human lower limb kinematics during running," in *Proc. Int. Tech. Meet. Sat. Div. Inst. Navig.*, Savannah, USA, Sept. 2008, pp. 1388-1397.
- [26] Y. Bar-Shalom, X. Li, and T. Kirubarajan, *Estimation with applications to Tracking and Navigation*, New York: Wiley, 2001.
- [27] D. Simon, *Optimal State Estimation: Kalman, H Infinity, and Nonlinear Approaches*, Hoboken, New Jersey: Wiley, 2006.
- [28] J. K. Lee, E. J. Park, and S. N. Robinovitch, "Estimation of attitude and external acceleration using inertial sensor measurement during various dynamic conditions," *IEEE Trans. Instrum. Meas.*, vol. 61, no. 8, pp. 2262-2273, Aug. 2012.
- [29] G. Agamennoni, J. I. Nieto, and E. M. Nebot, "Approximate inference in state-space models with heavy-tailed noise," *IEEE Trans. Sig. Proc.*, vol. 60, no. 10, pp. 5024-5037, Oct. 2012.
- [30] H. Nurminen, T. Ardeshiri, R. Piche, and F. Gustafsson "Robust inference for state-space models with skewed measurement noise," *IEEE Sig. Proc. Lett.*, vol. 22, no. 11, pp. 1898-1902, Nov. 2015.
- [31] A. H. Mohamed and K. P. Schwarz, "Adaptive Kalman filtering for INS/GPS," *Jour. Geod.*, vol. 73, pp. 193-203, 1999.
- [32] C. Hide, T. Moore, and M. Smith, "Adaptive Kalman filtering for low-cost INS/GPS," *Jour. Navig.*, vol. 56, pp. 143-152, 2003.
- [33] P. K. Yoon, S. Zihajehzadeh, B.-S. Kang and E. J. Park, "Adaptive Kalman Filter for Indoor Localization Using Bluetooth Low Energy and Inertial Measurement Unit", in *Proc. Ann. Int. Conf. IEEE Eng. Med. Bio. Soc. (EMBC)*, Milan, Italy, Aug. 2015, pp. 825-828.
- [34] P. K. Yoon, S. Zihajehzadeh, B.-S. Kang, and E. J. Park, "Robust Biomechanical Model-based Motion Tracking of Lower Body Using UWB and IMU," *IEEE Trans. Rob.*, submitted for publication (15-0624).

- [35] Q. Yuan, I-M. Chen, and S. P. Lee, "SLAC: 3D localization of human based on kinetic human movement capture," in *Proc. IEEE. Int. Conf. Rob. Aut.*, Shanghai, China, May 2011, pp. 848-853.
- [36] I. Skog, P. Handel, J.-O. Nilsson, and J. Rantakokko, "Zero-velocity detection—an algorithm evaluation," *IEEE Trans. Biomed. Eng.*, vol. 57, no. 11, pp. 2657-2666, Nov. 2010.
- [37] Q. Yuan and I-M. Chen, "Human velocity and dynamic behavior tracking method for inertial capture system," *Sens. Actuat. A: Phys.: Phys.*, vol. 183, pp. 123-131, June 2012.
- [38] G. Chang, "Robust Kalman filtering based on Mahalanobis distance as outlier judging criterion," *Jour. Geod.*, vol. 88, pp. 391-401, Jan. 2014.
- [39] G. Chang, Y. Wang, and Q. Wang, "Accuracy improvement by implementing sequential measurement update in robust Kalman filter," *Acta Geoda. Geophys.*, Jul. 2015.
- [40] M. Bloesch, S. Omari P. Fankhauser, H. Sommer, C. Gehring, J. Hwangbo, M. A. Hoepflinger, M. Hutter, and R. Siegwart, "Fusion of optical flow and inertial measurements for robust egomotion estimation," in *Proc. IEEE/RSJ Int. Conf. Intel. Rob. Syst.*, Chicago, USA, Sept. 2014, pp. 3102-3107.
- [41] F. M. Mirzaei and S. I. Roumeliotis, "A Kalman filter-based algorithm for IMU-camera calibration: observability analysis and performance evaluation," *IEEE Trans. Rob.*, vol. 24, no. 5, pp. 1143-1156, Oct. 2008.
- [42] A. Benini, A. Mancini, and S. Longhi, "An IMU/UWB/Vision-based extended Kalman filter for mini-UAV localization in indoor environment using 802.15.4a wireless sensor network," *Jour. Intel. Rob. Syst.*, vol. 70, pp. 461-476, 2013.
- [43] D. C. Montgomery, G. C. Runger, and N. F. Hubele, *Engineering Statistics*, Danvers: Wiley, 2010.
- [44] S. S. Bhattacharyya, E. F. Deprettere, R. Leupers, and J. Takala, *Handbook of Signal Processing Systems*, New York: Springer, 2010.
- [45] NOAA National Geophysical Data Center, "Earth's Magnetic Field Calculators", Internet: www.ngdc.noaa.gov/geomag/magfield [Oct. 25, 2015].

Appendix A.

Kalman Filter

The Kalman Filter (KF) can be deployed to estimate the state \mathbf{x} of the system that is governed by the linear stochastic difference equations [26], [27]:

$$\mathbf{x}_k = \mathbf{F}_{k-1}\mathbf{x}_{k-1} + \mathbf{G}_{k-1}\mathbf{u}_{k-1} + \mathbf{v}_{k-1} \quad (\text{A.1})$$

$$\mathbf{z}_k = \mathbf{H}_k\mathbf{x}_k + \mathbf{w}_k \quad (\text{A.2})$$

where \mathbf{F}_{k-1} and \mathbf{G}_{k-1} are the state transition and input matrices; \mathbf{u}_{k-1} is the input matrix; \mathbf{v}_{k-1} and \mathbf{w}_k are the process and measurement noise vectors; \mathbf{z}_k is the measurement vector; and \mathbf{H}_k is the observation matrix. The process noise \mathbf{v}_{k-1} and measurement noise \mathbf{w}_k are assumed to be independent, white, and normally distributed as following:

$$\mathbf{v}_{k-1} \sim N(0, \mathbf{Q}_k) \quad (\text{A.3})$$

$$\mathbf{w}_k \sim N(0, \mathbf{R}_k) \quad (\text{A.4})$$

where \mathbf{Q}_k and \mathbf{R}_k are the process and measurement noise covariance matrices.

The Kalman filter is consisted of following step ($k = 1, 2, \dots$):

- 1) Compute an *a priori* state estimate $\hat{\mathbf{x}}_k^-$

$$\hat{\mathbf{x}}_k^- = \mathbf{F}_{k-1}\hat{\mathbf{x}}_{k-1}^+ + \mathbf{G}_{k-1}\mathbf{u}_{k-1}. \quad (\text{A.5})$$

- 2) Compute an *a priori* error covariance matrix \mathbf{P}_k^-

$$\mathbf{P}_k^- = \mathbf{F}_{k-1}\mathbf{P}_{k-1}^+\mathbf{F}_{k-1}^T + \mathbf{Q}_{k-1}. \quad (\text{A.6})$$

- 3) Compute the Kalman gain \mathbf{K}_k

$$\mathbf{K}_k = \mathbf{P}_k\mathbf{H}_k^T(\mathbf{H}_k\mathbf{P}_k\mathbf{H}_k^T + \mathbf{R}_k)^{-1}. \quad (\text{A.7})$$

- 4) Compute an *a posteriori* state estimate $\hat{\mathbf{x}}_k^+$

$$\hat{\mathbf{x}}_k^+ = \hat{\mathbf{x}}_k^- + \mathbf{K}_k(\mathbf{z}_k - \mathbf{H}_k\hat{\mathbf{x}}_k^-). \quad (\text{A.8})$$

- 5) Compute an *a posteriori* error covariance matrix \mathbf{P}_k^+

$$\mathbf{P}_k^+ = \mathbf{P}_k^- - \mathbf{K}_k\mathbf{H}_k\mathbf{P}_k^-. \quad (\text{A.9})$$

For the post-processing, the Rauch-Tung-Striebel (RTS) smoother is applied to improve the position accuracy of the forward position estimate $\hat{\mathbf{x}}_k^+$ from the KF [26], [27].

- 1) Initialize an *a smoothed* state estimate $\hat{\mathbf{x}}_k$ and error covariance matrix $\hat{\mathbf{P}}_k$

$$\hat{\mathbf{x}}_k = \hat{\mathbf{x}}_k^+ \quad (\text{A.10})$$

$$\hat{\mathbf{P}}_k = \mathbf{P}_k^+. \quad (\text{A.11})$$

2) For $k = N - 1, \dots, 1, 0$, execute the following RTS smoother equations:

$$\mathbf{I}_{k+1}^- = (\mathbf{P}_{k+1}^-)^{-1} \quad (\text{A.12})$$

$$\mathbf{K}_k = \mathbf{P}_k^+ \mathbf{F}_k^T \mathbf{I}_{k+1}^- \quad (\text{A.13})$$

$$\hat{\mathbf{P}}_k = \mathbf{P}_k^+ - \mathbf{K}_k (\mathbf{P}_{k+1}^- - \hat{\mathbf{P}}_{k+1}) \mathbf{K}_k^T \quad (\text{A.14})$$

$$\hat{\mathbf{x}}_k = \hat{\mathbf{x}}_k^+ + \mathbf{K}_k (\hat{\mathbf{x}}_{k+1} - \hat{\mathbf{x}}_{k+1}^-). \quad (\text{A.15})$$

Appendix B.

Orientation Kalman Filter

Problem Definition

The 3D orientation is represented by the coordinate transformation of the 3×1 vector \mathbf{x} from the sensor frame S to the navigation frame N :

$${}^N\mathbf{x} = {}^N_S\mathbf{R} {}^S\mathbf{x}. \quad (\text{A.16})$$

where ${}^N\mathbf{x}$ and ${}^S\mathbf{x}$ are the vectors expressed in the navigation frame N and the sensor frame S , respectively. ${}^N_S\mathbf{R}$ is the rotation matrix of the sensor frame S with respect to the navigation frame N as expressed as

$${}^N_S\mathbf{R} = \begin{bmatrix} cac\beta & cas\beta s\gamma - sac\gamma & cas\beta c\gamma + sas\gamma \\ sac\beta & sas\beta s\gamma + cac\gamma & sas\beta c\gamma - cas\gamma \\ -s\beta & c\beta s\gamma & c\beta c\gamma \end{bmatrix} \quad (\text{A.17})$$

where c and s are cosine and sine functions, and α (yaw), β (pitch), and γ (roll) represent the orientation about the Z -, Y -, and X -axes of the navigation frame N , respectively. The rotation matrix ${}^N_S\mathbf{R}$ can also be represented with three unit column vectors as following:

$${}^N_S\mathbf{R} = [{}^S\mathbf{X} \quad {}^S\mathbf{Y} \quad {}^S\mathbf{Z}]^T \quad (\text{A.18})$$

The orientation KF deploys the attitude and yaw KFs to estimate 3D orientation using the IMU, consisted of triaxial accelerometer, triaxial gyroscope, and triaxial magnetometer [5]-[7], [28].

Attitude Kalman Filter

The attitude KF estimates the attitude (γ and β) by setting the unit column vector ${}^S\mathbf{Z}$ as the state. The last row of the matrix ${}^N_S\mathbf{R}$ (i.e. ${}^S\mathbf{Z} = [{}^S Z_1 \quad {}^S Z_2 \quad {}^S Z_3]^T$) can be expressed with only attitude (A.17). As a result, the states of the attitude KF are set to ${}^S\mathbf{Z}$, and the attitude are calculated using ${}^S\mathbf{Z}$ as following:

$$\gamma = \tan^{-1} \left(\frac{{}^S Z_2}{{}^S Z_3} \right) \quad (\text{A.19})$$

$$\beta = \tan^{-1} \left(\frac{-{}^S Z_1}{{}^S Z_2 / s\gamma} \right). \quad (\text{A.20})$$

The attitude is estimated by fusing the accelerometer and gyroscope signals in the KF structure (Appendix A). In the time update, the state is estimate with the gyroscope signal where the model is based on the first-order approximation of a strapdown integration. In the measurement update, the state is estimated with the accelerometer

signal by modelling the external acceleration ${}^N\mathbf{a}$ as a first-order low-pass filtered white noise process.

The attitude KF is governed by following linear stochastic equations:

$$\mathbf{x}_{1,k} = \mathbf{F}_{1,k-1}\mathbf{x}_{1,k-1} + \mathbf{v}_{1,k-1} \quad (\text{A.21})$$

$$\mathbf{z}_{1,k} = \mathbf{H}_{1,k}\mathbf{x}_{1,k} + \mathbf{w}_{1,k}. \quad (\text{A.22})$$

The transition matrix $\mathbf{F}_{1,k-1}$, the process noise $\mathbf{v}_{1,k-1}$ and the observation matrix $\mathbf{H}_{1,k}$ are derived as following:

$$\mathbf{F}_{1,k-1} = \mathbf{I} - \Delta t \tilde{\mathbf{y}}_{G,k-1} \quad (\text{A.23})$$

$$\mathbf{v}_{1,k-1} = \Delta t (-\tilde{\mathbf{x}}_{1,k-1}) \mathbf{n}_G \quad (\text{A.24})$$

$$\mathbf{H}_{1,k} = g\mathbf{I} \quad (\text{A.25})$$

where \mathbf{I} is the identity matrix, Δt is the sampling period, and $\tilde{\mathbf{y}}_{G,k-1}$ is a skew symmetric matrix of triaxial gyroscope measurements. $\tilde{\mathbf{x}}_{1,k-1}$ is the skew symmetric matrix of previous *a posteriori* state vector, \mathbf{n}_G is the uncorrelated measurement noise with zero-mean white Gaussian, and g ($= 9.81 \text{ m/s}^2$) is the gravity.

The measurement vector $\mathbf{z}_{1,k}$ can be calculated as following:

$$\mathbf{z}_{1,k} = \mathbf{y}_{A,k} - c_a {}^S\mathbf{a}_{k-1}^+ \quad (\text{A.26})$$

where $\mathbf{y}_{A,k}$ is the triaxial accelerometer measurements, \mathbf{a}_{k-1} is the gravity compensated external acceleration, and c_a is the dimensionless constant between 0 and 1 which determines the cut-off frequency in the external acceleration model.

The process noise covariance matrices $\mathbf{Q}_{1,k-1}$ and measurement noise covariance matrices $\mathbf{R}_{1,k}$ are calculated as following:

$$\mathbf{Q}_{1,k-1} = -\Delta t^2 \tilde{\mathbf{x}}_{1,k-1} \Sigma_G \tilde{\mathbf{x}}_{1,k-1} \quad (\text{A.27})$$

$$\mathbf{R}_{1,k} = \Sigma_{acc} + \Sigma_A \quad (\text{A.28})$$

where Σ_G is the covariance matrix of the gyro's measurement noise. Σ_{acc} is the covariance matrix of the acceleration model error, and Σ_A is the covariance matrix of the accelerometer's measurement noise. Σ_G , Σ_{acc} , and Σ_A are calculated as following:

$$\Sigma_G = \sigma_G^2 \mathbf{I} \quad (\text{A.29})$$

$$\Sigma_{acc} = 1/3 c_a^2 \| {}^S\mathbf{a}_{k-1}^+ \|^2 \mathbf{I} \quad (\text{A.30})$$

$$\Sigma_A = \sigma_A^2 \mathbf{I} \quad (\text{A.31})$$

where σ_A^2 is the accelerometer noise variance, and σ_G^2 is the gyro noise variance.

Once the *a posteriori* state vector ${}^S\hat{\mathbf{z}}_k^+$ is estimated, the external acceleration ${}^S\mathbf{a}_k^+$ is

obtained by

$${}^S\mathbf{a}_k^+ = \mathbf{y}_{A,k} - g\hat{\mathbf{x}}_{1,k}^+ \quad (\text{A.32})$$

Compared to the other existing attitude algorithms, this attitude KF is particularly designed for the dynamic conditions where the external acceleration is present [28]. The performance of the attitude KF has been validated on the experimental tests in various dynamic condition settings with average reference external acceleration ranging from 0.40 to 6.29 m/s² [28]. This algorithm is suitable for the applications where the dynamic activities, especially on the jumping and running, frequently result in large external accelerations.

Yaw Kalman Filter

The yaw KF estimates the yaw by setting the unit column vector ${}^S\mathbf{X}$ ($= [{}^SX_1 \quad {}^SX_2 \quad {}^SX_3]^T$) as the state vector. The yaw is calculated using the estimated attitude (i.e. β and γ) from the attitude KF and the state as following:

$$\alpha = \tan^{-1}\left(\frac{-c\gamma {}^SX_2 + s\gamma {}^SX_3}{{}^SX_1/c\beta}\right). \quad (\text{A.33})$$

The states of the yaw KF are set to ${}^S\mathbf{X}$. The yaw is estimated by fusing the gyroscope and magnetometer signal in the KF structure [5], [7]. Similar to the attitude KF, the state is first estimated with the gyroscope signal where the model is based on the first-order approximation of a strapdown integration. In the measurement model, using the estimated roll and pitch from the attitude KF, the triaxial magnetometer measurements are rotated to the horizontal plane of the navigation frame N . The yaw is estimated from the magnetometer signal in the horizontal component of the navigation frame N .

The yaw KF is governed by following equations:

$$\mathbf{x}_{2,k} = \mathbf{F}_{2,k-1}\mathbf{x}_{2,k-1} + \mathbf{v}_{2,k-1} \quad (\text{A.34})$$

$$\mathbf{z}_{2,k} = \mathbf{H}_{2,k}\mathbf{x}_{2,k} + \mathbf{w}_{2,k} \quad (\text{A.35})$$

where $\mathbf{F}_{2,k-1}$ and $\mathbf{w}_{2,k-1}$ are equal to $\mathbf{F}_{2,k-1}$ and $\mathbf{w}_{2,k-1}$ used in the attitude KF. $\mathbf{H}_{2,k}$ is set as \mathbf{I} . $\mathbf{Q}_{2,k-1}$ is same as $\mathbf{Q}_{1,k-1}$ used in the attitude KF.

Prior to estimating yaw with the yaw KF, the sensor frame first needs to be rotated to navigation frame N in the horizontal plane with a rotation matrix ${}^N_S\mathbf{R}_{\beta,\gamma}$ with respect to the horizontal plane constructed from the estimated β and γ from attitude KF as following:

$${}^N_S\mathbf{R}_{\beta,\gamma} = \begin{bmatrix} c\beta & s\beta s\gamma & s\beta c\gamma \\ 0 & c\gamma & -s\gamma \\ -s\beta & c\beta s\gamma & c\beta c\gamma \end{bmatrix}. \quad (\text{A.36})$$

The triaxial magnetometer signals \mathbf{y}_M are rotated to a horizontal plane using the rotation matrix ${}^N_S\mathbf{R}_{\beta,\gamma}$ as below. The rotated signal are expressed with $\mathbf{y}_M^{\beta,\gamma}$.

$$\mathbf{y}_M^{\beta,\gamma} = {}^N_S\mathbf{R}_{\beta,\gamma}\mathbf{y}_M \quad (\text{A.37})$$

The yaw α_M can be estimated as an angle between the magnetometer signals in a horizontal plane $\mathbf{y}_M^{\beta,\gamma} (= [x_M^{\beta,\gamma} \ y_M^{\beta,\gamma}]^T)$ and the Earth's magnetic field in a horizontal plane $\mathbf{m}_f (= [m_{f,x} \ m_{f,y}]^T)$, which is based on the latitude and longitude of the object location in North. \mathbf{m}_f is manually set in the beginning of test and can be looked up in the geographic scientific agency webpage [45].

$$\alpha_M = -\tan^{-1}\left(\frac{y_M^{\beta,\gamma}}{x_M^{\beta,\gamma}}\right) + \tan^{-1}\left(\frac{m_{f,y}}{m_{f,x}}\right) = -\tan^{-1}\left(\frac{\mathbf{y}_M^{\beta,\gamma} \times \mathbf{m}_f}{\mathbf{y}_M^{\beta,\gamma} \cdot \mathbf{m}_f}\right). \quad (\text{A.38})$$

With the estimated yaw from the above equation, the measurement vector $\mathbf{z}_{2,k}$ is formed first column of the rotation matrix as discussed. It is constructed with estimated β and γ from attitude KF and the yaw α_M from (A.38) as following:

$$\mathbf{z}_{2,k} = [{}^S X_1 \quad {}^S X_2 \quad {}^S X_3]^T = [c\alpha_M c\beta \quad c\alpha_M s\beta s\gamma - s\alpha_M c\gamma \quad c\alpha_M s\beta c\gamma + s\alpha_M s\gamma]^T. \quad (\text{A.39})$$

In an indoor environment, the magnetometer signals are commonly contaminated with the magnetic disturbance due to ferrous metal. The following criteria are implemented in order to detect the perturbed situations [5], [7]:

$$\mathbf{R}_M = \begin{cases} \sigma_M^2 \mathbf{I}, & \text{if } \|\mathbf{y}_M\| - \|\mathbf{m}_{t=0}\| \leq \varepsilon_M \\ \infty \mathbf{I}, & \text{otherwise} \end{cases} \quad (\text{A.40})$$

where \mathbf{R}_M is the measurement noise covariance of the yaw KF, σ_M^2 is the magnetometer noise variance, $\mathbf{m}_{t=0}$ is the Earth's magnetic field, and ε_M is the threshold to detect the ferromagnetic disturbance. Upon the magnetic disturbance, the norm of the magnetometer signal strongly deviates from the norm of the Earth's magnetic field. As a result, the gyroscope signal is used for estimating the yaw. Otherwise, the yaw is estimated from both gyroscope and magnetometer signals.

The structure of the proposed orientation algorithm is shown in Figure A.1.

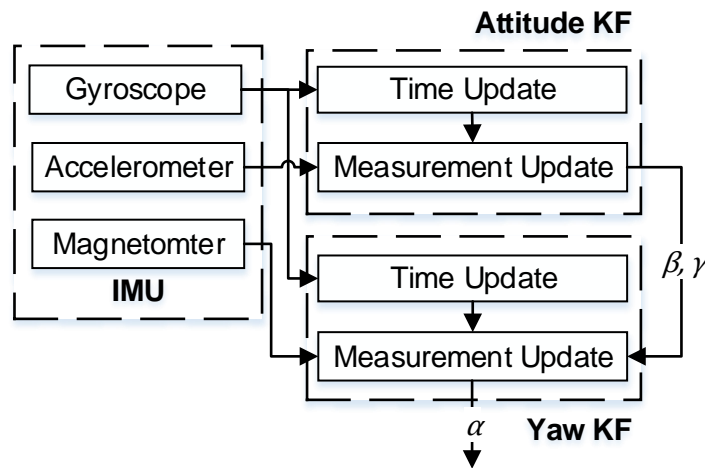


Figure A.1. Overview of the orientation algorithm structure

Appendix C.

Rotation and Homogenous Transformation

For two coordinate systems A, B , the homogenous transformation ${}^A_B\mathbf{T}$ is represented as following:

$${}^A_B\mathbf{T} = \begin{bmatrix} {}^A_B\mathbf{R} & {}^A\mathbf{P}_B \\ \mathbf{0}_{1 \times 3} & 1 \end{bmatrix} \quad (\text{A.41})$$

where ${}^A\mathbf{P}_B$ is the position vector of origin of the frame B with respect to frame A .

Both rotation ${}^B_A\mathbf{R}$ and transformation ${}^B_A\mathbf{T}$ matrices can be inverted as following:

$${}^B_A\mathbf{R} = {}^A_B\mathbf{R}^T \quad (\text{A.42})$$

$${}^B_A\mathbf{T} = ({}^A_B\mathbf{T})^{-1} = \begin{bmatrix} {}^A_B\mathbf{R}^T & -({}^A_B\mathbf{R}^T)({}^A\mathbf{P}_B) \\ \mathbf{0}_{1 \times 3} & 1 \end{bmatrix}. \quad (\text{A.43})$$

Both transformation ${}^0_n\mathbf{T}$ and rotation ${}^0_n\mathbf{R}$ matrices can be compounded as following:

$${}^0_n\mathbf{T} = ({}^0_1\mathbf{T})({}^1_2\mathbf{T}) \dots ({}^{n-2}_{n-1}\mathbf{T})({}^{n-1}_n\mathbf{T}) \quad (\text{A.44})$$

$${}^0_n\mathbf{R} = ({}^0_1\mathbf{R})({}^1_2\mathbf{R}) \dots ({}^{n-2}_{n-1}\mathbf{R})({}^{n-1}_n\mathbf{R}). \quad (\text{A.45})$$

Appendix D.

Ethics Approval



Street Address
Simon Fraser University
Discovery 2
Room 230, 8900 Nelson Way
Burnaby, BC Canada V5A 4W9

Mailing Address
8888 University Drive
Discovery 2
Burnaby, BC Canada
V5A 1S6

Director 778.782.6593
Associate Director 778.782.9631
Manager 778.782.3447
dore@sfu.ca
<http://www.sfu.ca/ore>

Annual Renewal Approval

Study Number: 2013s0750

Study Title: Wireless Inertial Sensor Network for Ubiquitous Motion Capture

Annual Renewal Date: Oct. 23, 2014

Expiry Date: Oct. 25, 2015

Principal Investigator: Park, Edward

Supervisor: na

SFU Position: Faculty

Faculty/Department: School of Mechatronic
Systems Engineering

Co-Investigators/Research Personnel: Ivan Bajic, Choong Hoon Kwak, Matthew Lee, Daniel Lee, Darrell Loh, Magnus Musngi, Gopi Raju, Mehdi Stapleton, Paul Yoon, Ali Zarel Ghanavati, and Shaghayegh Zihajehzadeh.

Funding Source 1: NSERC

Grant Title 1: Wireless inertial sensor network for ubiquitous human motion capture

Approved in this Application:

- Annual Renewal/Progress Report Form
- Annual Renewal Approval Expiry Date to Oct. 25, 2015

The approval for the above-referenced study expires on the **Expiry Date**. **Failure to submit an annual renewal form will lead to your study being suspended and potentially terminated.** If you intend to continue your protocol to collect data past the term of approval, you must submit an annual renewal/progress report at least 4 weeks before the expiry date at dore@sfu.ca.

Please notify the Office of Research Ethics at dore@sfu.ca once you have completed the data collection portion of your project so that we can close the file.



OFFICE OF RESEARCH ETHICS

This Notification of Status is your official Annual Renewal Approval documentation for this project. Please keep this document for reference purposes.

Sincerely,

Dina Shafey, MBA, PhD
Acting Associate Director,
Office of Research Ethics

Page 2 of 2